

1 Global 1km Land Surface Parameters for Kilometer-Scale Earth System Modeling

2 Lingcheng Li, Gautam Bisht, Dalei Hao, L. Ruby Leung

3 Atmospheric, Climate, and Earth Sciences, Division, Pacific Northwest National Laboratory,
4 Richland, WA, USA

Deleted: and Global Change

5

6 Correspondence: Lingcheng Li (lingcheng.li@pnnl.gov) and Gautam Bisht
7 (gautam.bisht@pnnl.gov)

8

10 **Abstract**

11 Earth system models (ESMs) are progressively advancing towards the kilometer scale (k-scale).
12 However, the surface parameters for Land Surface Models (LSMs) within ESMs running at the k-
13 scale are typically derived from coarse resolution and outdated datasets. This study aims to develop
14 a new set of global land surface parameters with a resolution of 1 km for multiple years from 2001
15 to 2020, utilizing the latest and most accurate available datasets. Specifically, the datasets consist
16 of parameters related to land use and land cover, vegetation, soil, and topography. [Differences](#)
17 [between the newly developed 1k land surface parameters and conventional parameters emphasize](#)
18 [their potential for higher accuracy due to the incorporation of the most advanced and latest data](#)
19 [sources.](#) To demonstrate the capability of these new parameters, we conducted 1 km resolution
20 simulations using the E3SM Land Model version 2 (ELM2) over the contiguous United States.
21 Our results demonstrate that land surface parameters contribute to significant spatial heterogeneity
22 in ELM2 simulations of soil moisture, latent heat, emitted longwave radiation, and absorbed
23 shortwave radiation. On average, about 31% to 54% of spatial information is lost by upscaling the
24 1 km ELM2 simulations to a 12 km resolution. Using eXplainable Machine Learning (XML)
25 methods, the influential factors driving the spatial variability and spatial information loss of ELM2
26 simulations were identified, highlighting the substantial impact of the spatial variability and
27 information loss of various land surface parameters, as well as the mean climate conditions. The
28 new land surface parameters are tailored to meet the emerging needs of k-scale LSMs and ESMs
29 modeling with significant implications for advancing our understanding of water, carbon, and
30 energy cycles under global change. The 1 km land surface parameters are publicly available at
31 <https://doi.org/10.25584/PNNLDH/1986308> (Li et al., 2023).

Formatted: Default Paragraph Font

Formatted: Font color: Auto

32 **1. Introduction**

33 Aided by advancements in computing power, it has become increasingly feasible to run land
34 surface models (LSMs) and Earth system models (ESMs) at the kilometer scale (k-scale) to
35 improve our understanding of Earth system processes. The emergence of k-scale modeling has the
36 potential to improve the accuracy of climate simulations significantly and allow for explicit
37 modeling of physical processes that were previously poorly represented in climate models (Nat.
38 Clim. Chang. 2022), such as modeling of mesoscale convective systems in the atmosphere (Slingo
39 et al., 2022) and mesoscale eddies in ocean (Hewitt et al., 2022). Simultaneously, land modeling
40 has also witnessed a surge of interest in hyper-resolution modeling, initially proposed by Wood et
41 al. (2011), which aims to model land surface processes at a horizontal resolution of 1 km globally
42 and 100 m or finer for continental or regional domains. The motivation behind hyper-resolution
43 modeling is to address the requirements of operational forecasting like extreme events, and to
44 enhance our understanding of hydrological and biogeochemical cycling, and land-atmosphere
45 interactions. High-resolution LSMs have been increasingly applied in various fields, as
46 demonstrated by recent examples, such as 30-meter soil moisture simulations over the contiguous
47 United States (CONUS) (Vergopolan et al., 2020, 2021, 2022), 500-meter hyper-resolution
48 modeling of surface and root zone soil moisture over Oklahoma (Rouf et al., 2021), 1-km
49 simulations over Southwestern US (Singh et al., 2015), 3-km simulations over eastern Tibetan
50 Plateau to understand hydrological changes over mountainous regions (Yuan et al., 2018; Ji and
51 Yuan, 2018), 6-km simulations over China to reduce simulations errors of hydrological variables
52 (Ji et al., 2023). High-resolution modeling can better capture the land surface heterogeneity and

53 could improve simulations of terrestrial water, ~~and energy cycles (Giorgi and Avissar, 1997;~~

54 ~~Chaney et al., 2018; Xu et al., 2023), biogeochemical cycles, (Chaney et al., 2018), as well as land-~~

Deleted: ,

Deleted: , and

Deleted: ,

Deleted: and

59 atmosphere coupling (Liu et al., 2017; Zhou et al., 2019; Bou-Zeid et al., 2020). For example,
60 Singh et al. (2015) demonstrated that increasingly capturing topography and soil texture
61 heterogeneity at finer resolutions (e.g., 1 km) improves land surface modeling of water and energy
62 variables. Li et al. (2022) have shown that the spatial heterogeneities of land surface parameters
63 (including land use and land cover (LULC) and topography) are essential for modeling the spatial
64 variability of land surface energy and water partitioning. Hao et al. (2022) found that 1 km
65 simulations with sub-grid topographic configurations can better capture the topographic effects on
66 surface fluxes.

Deleted: (Giorgi and Avissar, 1997; Chaney

Deleted: 2018

Deleted: Liu et al., 2017;

Deleted: ; Chen et al., 2020; Nitta et al., 2020; Vrese et al., 2016).

67
68 The parameters for LSMs within ESMS being run at the k-scale are typically derived from coarse
69 resolution datasets or outdated datasets. Consequently, k-scale modeling may not accurately
70 represent fine-scale land surface heterogeneity unless high-resolution land surface parameters at
71 the kilometer or finer scales are utilized. Publicly available land surface parameters are primarily
72 provided at coarse resolutions and based on outdated datasets (see details in Table 1). For example,

Deleted:

73 the Community Land Model version 5 (CLM5; Lawrence et al., 2019) typically relies on land
74 surface parameters with spatial resolutions ranging from 1km to 0.5° based on source datasets that
75 were processed more than 10 years ago (see Table 1 for details). Although LULC-related
76 parameters are available at a relatively high resolution of 0.05°, they are temporally static and were
77 derived from a combination of data from different years spanning 1993 to 2012 (Table 1). Leaf
78 area index (LAI) was derived from the now outdated products of Moderate Resolution Imaging
79 Spectroradiometer (MODIS) collection 4 (Myneni et al., 2002). The canopy height for tree Plant
80 Functional Types (PFTs) is based on forest canopy height data derived from the Geoscience Laser
81 Altimeter System (GLAS) aboard ICESat, collected in 2005 (Simard et al., 2011). Canopy height

Deleted: .

Formatted: Font color: Text 1

Formatted: Font color: Text 1

Formatted: Font color: Text 1

89 for short vegetation is represented by PFT-specific values that remain invariant in space (Bonan et
90 al., 2002). Soil sand and clay content were obtained from the International Geosphere-Biosphere
91 Programme (IGBP) soil dataset (Global Soil Data Task 2000) consisting of 4931 soil mapping
92 units (IGBP, 2000). These CLM5 land surface parameters have been widely utilized in the LSMs
93 and ESMs communities, despite being developed over a decade ago. Subsequently, Ke et al. (2012;
94 hereafter referred to as K2012) developed an updated set of LULC and vegetation-related land
95 surface parameters for CLM4 at a resolution of 0.05°. These parameters were developed based on
96 MODIS collection 5 products or datasets derived from MODIS collection 5 products, including
97 PFTs and non-vegetation land cover, LAI, and Stem Area Index (SAI). K2012 has also been widely
98 used by LSMs, including CLM (e.g., Leng et al., 2013; ~~Ke et al., 2013~~; Singh et al., 2015; Xia et
99 al., 2017) and the Energy Exascale Earth System Model (E3SM) Land Model (ELM) (e.g.,
100 Caldwell et al., 2019; Leung et al., 2020; Li et al., 2022). However, the CLM5 and K2012 datasets,
101 with their relatively coarse resolution and reliance on outdated data from over a decade ago, may
102 not fully meet the requirements for k-scale modeling. Additionally, these datasets include LULC,
103 LAI, and SAI that are year invariant. Consequently, they are inappropriate for studies involving
104 LULC changes, such as urbanization. In addition, some recently developed land surface processes
105 and their associated parameters are not included in previous datasets. For instance, Hao et al. (2021)
106 introduced a sub-grid topographic parameterization of solar radiation with five associated
107 topographic factors in ELM, which have been found to significantly affect the surface energy
108 budget. the surface energy budget.

109
110 High-resolution and up-to-date datasets at kilometer or finer resolutions are now widely available
111 and can be utilized to derive more accurate land surface parameters for k-scale LSM simulations.

Formatted: Font color: Text 1

Deleted: community

Formatted: Font color: Text 1

Deleted: ; Ke et al., 2013

Formatted: Font color: Text 1

Formatted: Font color: Text 1

Formatted: Font color: Text 1

Formatted: Font color: Text 1

114 For example, the MODIS Land Cover Type Collection 6 (MCD12Q1 C6) data product provides
115 global land cover types yearly from 2001 to the present (Friedl et al., 2019; Sulla-Menashe et al.,
116 2019) at 500-meter resolution. Compared to the MODIS Collection 4 (used in CLM5 land surface
117 parameters) and Collection 5 products (used in K2012 land surface parameters), the C6 data
118 represents a significant advancement in algorithm improvements and the quality of land cover
119 information. Despite the availability of high-resolution MODIS LAI products, such as the 500 m
120 MCD15A2H (Myneni et al., 2021), they suffer from noise and gaps with spatially and temporally
121 inconsistent values due to clouds, seasonal snow cover, instrument issues, and uncertainties in
122 retrieval algorithms (Yuan et al., 2011). To address these limitations, Yuan et al. (2011)
123 reprocessed MODIS LAI products and generated a more accurate and spatiotemporally continuous
124 and consistent LAI dataset that is available continuously to the present period. Additional high-
125 resolution and up-to-date datasets are available for preparing land surface parameters, such as soil
126 texture and soil organic matter at 250-meter resolution (Poggio et al., 2021) and vegetation height
127 at 10-m resolution (Lang et al., [2023](#)).

Deleted: 2022

128
129 This study aims to develop a new set of global land surface parameters with a resolution of 1 km
130 for multiple years, utilizing the latest and most accurate available datasets. These parameters will
131 be tailored to meet the needs of k-scale Earth system modeling. The newly developed land surface
132 parameters include four categories: (1) LULC-related parameters, such as the spatial distributions
133 of PFTs, lakes, wetlands, urban areas, and glaciers; (2) vegetation-related parameters, including
134 PFTs' LAI and SAI for multiple years ranging from 2001 to 2021, and the canopy top and bottom
135 height; (3) soil-related parameters, such as soil textures and soil organic matter; and (4)
136 topography-related parameters, such as [elevation](#), slope, aspect, and sub-grid topographic factors.

138 ~~We conducted a comparison of the new 1k parameters against the K2012 and ELM2/CLM5 default~~
139 ~~parameters. Utilizing~~ ELM version 2 (ELM2) as a testbed, ~~we demonstrated the modeling~~
140 capability ~~enabled by~~ the new high-resolution parameters ~~through~~ a 5-year ~~simulation at 1 km~~
141 resolution ~~over the CONUS. We performed a spatial scaling analysis on four ELM2 simulated~~
142 variables, which included soil moisture, latent heat, emitted longwave radiation, and absorbed
143 shortwave radiation, to underscore the significance of high-resolution land surface parameters on
144 ELM2 simulations. We employed eXplainable Machine Learning (XML) methods to evaluate the
145 most important factors of land surface parameters and climate conditions (e.g., mean temperature
146 and precipitation) in driving the spatial variability and spatial information loss of ELM2
147 simulations.

Deleted: We employed the

Deleted: to demonstrate

Deleted: of

Deleted: by conducting

Deleted: simulation

153 **2. Development of 1km land surface parameters**

154 In this study, all the land surface parameters were developed globally at a resolution of
155 approximately 1 km (i.e., 1/120°, hereafter referred to as 1 km; Table 1). The LULC-related
156 parameters, soil properties, canopy height, and elevation were processed via Google Earth Engine
157 (GEE; Gorelick et al., 2017). The LAI was processed using an area-weighted average from its
158 original 450 m resolution obtained from Beijing Normal University (Yuan et al., 2011). [All data](#)
159 [sources utilized in this study have been rigorously validated in their respective original](#)
160 [publications.](#) The detailed methods for deriving these parameters are described below.

161

Table 1 Comparison between new and previous land surface parameters

Category	Land surface parameters	This study	ELM2 / CLM5 *	K2012
LULC	PFTs, Lake, Glacier, Urban	<ul style="list-style-type: none"> Resolution: 1 km, yearly, 2001-2020 Data source: 500 m, yearly, MODIS collection 6 (Friedl et al., 2019) 	<ul style="list-style-type: none"> Resolution: 0.05°, temporally static, processed based on data from mixed years PFTs data source: mixed years from 1993 to 2001; 500 m, MODIS Vegetation Continuous Fields (Hansen et al., 2003); 1 km, tree cover (Defries et al., 2000); 10 km (5 arc minutes), cropland (Ramankutty and Foley, 1999); 1 km, MODIS land cover collection 4 (Friedl et al., 2002) Lake data source: 3 km (90 arc seconds) lake data (Kourzeneva 2009, 2010) Glacier data source: glacier and ice sheet vector data (Arendt et al. 2012; Rastner et al. 2012) Urban data source: 1 km urban data (Jackson et al., 2010) 	<ul style="list-style-type: none"> Resolution: 0.05°, year 2005 Data source: 500 m, yearly, MODIS collection 5 (Friedl et al., 2010)
	LAI, SAI	<ul style="list-style-type: none"> Resolution: 1 km, monthly, 2001-2020 Data source: 450 m, 8-day, reprocessed MODIS collection 6 LAI (Yuan et al., 2011; Friedl et al., 2019) 	<ul style="list-style-type: none"> Resolution: 0.5°, 12 months Data source: 1 km, 8-day, MODIS collection 4 LAI (Myneni et al., 2002) 	<ul style="list-style-type: none"> Resolution: 0.05°, year 2005 Data source: 450 m, 8-day, reprocessed MODIS collection 5 LAI (Yuan et al., 2011; Friedl et al., 2010)
Vegetation	Canopy top height, Canopy bottom height	<ul style="list-style-type: none"> Resolution: 1 km, temporally static Data source: 10 m, vegetation canopy height (Lang et al., 2023) 	<ul style="list-style-type: none"> Resolution: 0.5° or PFT specified value, temporally static Tree PFT data source: 1 km, forest canopy height derived using 2005 GLAS aboard ICESat data (Simard et al., 2011); Short vegetation data source: PFT specific values (Bonan et al., 2002) 	--
	Percent sand, Percent clay	<ul style="list-style-type: none"> Resolution: 1 km, temporally static Data source: 250 m, Soilgrid v2 (Poggio et al., 2021) 	<ul style="list-style-type: none"> Resolution: 10 km (0.083°), temporally static Data source: IGBP soil data of 4931 mapping units (IGBP, 2000) 	--
Soil	Soil organic matter	<ul style="list-style-type: none"> Resolution: 1 km, temporally static Data source: 90 m, MERIT Hydro elevation (Yamazaki et al., 2019) 	<ul style="list-style-type: none"> Resolution: merge of 1 km and 10 arc minutes, temporally static Data source: global most regions are based on USGS HYDRO1k (Verdin and Greenlee 1996; but 10 arc minute data is used over Greenland and Antarctica. 	--
	Elevation, Slope, Standard deviation of elevation	<ul style="list-style-type: none"> Resolution: 1 km, temporally static Data source: 90 m, MERIT Hydro elevation (Yamazaki et al., 2019) 	<ul style="list-style-type: none"> Resolution: 1 km, temporally static Data source: 90 m, MERIT Hydro elevation (Yamazaki et al., 2019) 	--
Topography	Aspect, Sky view factor, Terrain configuration factor	<ul style="list-style-type: none"> Resolution: 1 km, temporally static Data source: 90 m, MERIT Hydro elevation (Yamazaki et al., 2019) 	--	--

Formatted Table

Deleted: 2022

Deleted: 2022

Deleted: 2022

Split Cells

Split Cells

Moved (insertion) [1]

Deleted:)

Deleted: ¶ Slope ... [1]

Moved up [1]: Standard deviation of elevation

Deleted: ¶ Aspect ... [2]

163 * ELM2 and CLM5 share the same default land surface parameters, detailed descriptions available at:
 164 https://escomp.github.io/ctsm-docs/versions/release-clm5.0/html/tech_note/index.html.

176 **2.1 LULC-related parameters**

177 In this study, the MODIS MCD12Q1 version 6 (Friedl et al., 2022) was employed to ascertain the
178 Plant Functional Types (PFT) as well as other non-vegetative land categories at a spatial resolution
179 of 1 km spanning the years 2001 to 2020. The integrity of the MODIS land cover product has been
180 established through a 10-fold cross-validation accuracy assessment using the Terrestrial
181 Ecosystem Parameterization database (Sulla-Menashe et al., 2019). This land cover product offers
182 richer and more flexible land cover data with higher accuracy and substantially less year-to-year
183 stochastic variation in classification results (Sulla-Menashe et al., 2019). Being the sole operational
184 global land cover product available with annual intervals, it addresses a significant gap in the realm
185 of global change research.

Deleted: This study utilized MODIS MCD12Q1 version 6 (Friedl et al., 2022) to derive the PFT and other non-vegetation land types at a resolution of 1 km for 2001–2020.

186
187 The original MODIS land cover data was first resampled to 1 km from its original 500 m resolution
188 using a majority resampling method in GEE. At such a high 1km resolution, we did not consider
189 the proportion of different land cover types within each grid. Instead, we assigned 100% of a grid
190 cell to the major land cover type. Specifically, the MCD12Q1 LC_Type 5 PFT classification layer
191 was used to determine the distributions of the seven PFTs, as well as lake, urban, and glacier,
192 following the method outlined in Ke et al. (2012) and summarized below:

193 • The seven PFTs include needleleaf evergreen trees, needleleaf deciduous trees, broadleaf
194 evergreen trees, broadleaf deciduous trees, shrub, grass, and crop. These PFTs were further
195 reclassified into 15 categories (Table S1) that are typically used in LSMs based on the rules
196 presented in Bonan et al. (2002a) with the assistance of 1 km precipitation and surface air
197 temperature from WorldClim V1 (Hijmans et al., 2005).

Deleted: (NET),

Deleted: (NDT),

Deleted: (BET),

Deleted: (BDT),

Deleted: (SHR),

Deleted: (GRS),

Deleted: (CRO).

208 • Grass was reclassified as C3 and C4 grass using the approach presented by Still et al. (2003),
209 with the assistance of monthly LAI (processed in section 2.2.1) and meteorological
210 variables from WorldClim V1.

211 • The "non-vegetated land" was classified as barren soil class.

212 • The "permanent snow and ice" was assigned as the glacier land unit.

Deleted:

213 • Global lakes were identified based on the classification of "water bodies" over the global
214 land, constrained using the global land mask obtained from Natural Earth
215 (<https://www.naturalearthdata.com/>).

216 • The urban land unit was determined based on the MODIS "urban and built-up"
217 classification. These urban grids were further classified into three urban classes, namely,
218 tall building district (TBD), high density (HD), and medium density (MD), based on
219 Jackson et al. (2010; hereinafter referred to as J2010). J2010 generated global urban extent
220 maps for the TBD, HD, and MD classes at a spatial resolution of 1 km, based on rules of
221 building height and vegetation coverage fraction
222 (https://gdex.ucar.edu/dataset/188a_oleson/file.html). However, the J2010 dataset is
223 temporally static and cannot reflect changes in urban boundaries over time. Therefore, we
224 reclassified the yearly MODIS urban land class as TBD, HD, and MD based on the J2010
225 dataset using the nearest neighbor sampling method for each year.

226 After determining the distribution of 15 PFTs, bare soil, lake, glacier, and urban land, any
227 remaining 1 km grids were assigned as ocean (Table S1). It should be noted that the wetland land
228 unit was not explicitly classified in this study. This is because, instead of treating wetlands as an
229 individual land unit, many LSMs (e.g., ELM2 and CLM5) integrate wetland functioning processes

231 prognostically within other land units where a surface water storage component is implemented to
232 represent wetland functioning.

233

234 2.2 Vegetation-related parameters

235 2.2.1 Monthly LAI and SAI

236 The monthly LAI parameters were obtained from Beijing Normal University (BNU_LAI; Yuan et

237 al., 2011). BNU_LAI, ~~an enhanced~~ version of the MODIS LAI product, has ~~been subjected to~~

238 ~~thorough~~ quality control, ~~incorporating~~ multiple algorithms ~~for improved accuracy~~ (Yuan et al.,

239 2011). ~~Its validation involved an extensive array of LAI reference maps and employed the bottom-~~

240 ~~up approach advocated by the CEOS Land Product Validation sub-group (Morisette et al., 2006).~~

241 ~~Compared to~~ the original MODIS LAI, ~~the BNU LAI dataset exhibits superior performance, along~~

242 ~~with enhanced spatiotemporal continuity and consistency.~~ The 8-day BNU_LAI product at a

243 resolution of 15 seconds (~450 m) over 2001–2020 was downloaded from

244 <http://globalchange.bnu.edu.cn/research/laiV061>. Subsequently, the data were resampled to a

245 resolution of 1 km using an area-weighted average method and averaged temporally for each

246 month. The processed monthly LAI at 1 km resolution was subsequently assigned to each of the

247 15 PFTs described above at each grid. The monthly SAI was then calculated based on the

248 processed monthly LAI using the methods and PFT parameters described in Zeng et al. (2002).

249

250 2.2.2 Vegetation canopy height

251 ~~We leveraged a~~ global vegetation canopy height dataset ~~sourced~~ from Lang et al. (2023). ~~This~~

252 ~~dataset, derived using~~ a probabilistic deep learning model, ~~fuses~~ Sentinel-2 images ~~with the~~ Global

253 Ecosystem Dynamics Investigation (GEDI) ~~to retrieve canopy height. It stands out as the inaugural~~

Deleted: is a reprocessed

Deleted: C6

Deleted: which

Deleted: undergone comprehensive

Deleted: and use of

Formatted: Font color: Text 1

Deleted:). The data have better performance in

Deleted: against

Deleted: LAI and are more spatiotemporally continuous and consistent than

Deleted: (Yuan et al., 2011).

Formatted: Font color: Text 1

Deleted: The

Deleted: used in this study was obtained

Deleted: (2022). Lang et al. (2022) developed

Deleted: to retrieve canopy height from the

Deleted: by fusing

Deleted:). This dataset is

Deleted: first globally

271 global canopy height dataset offering consistent, wall-to-wall coverage at a 10 m spatial resolution
272 across all vegetation types. Assessments using hold-out GEDI reference data and comparisons
273 with independent airborne LiDAR data demonstrate that the approach outlined by Lang et al. (2023)
274 produces a meticulously quality-controlled, state-of-the-art global map product, accompanied by
275 quantitative uncertainty estimates. The canopy height served as the canopy top height parameter.
276 Canopy bottom height was calculated by multiplying PFT-based ratios derived from the ratio of
277 ELM2's (same as CLM5) canopy top and bottom heights for different PFTs (Table S2).

Deleted: and

Deleted: canopy height

Deleted: and includes canopy height for

278

279 2.3 Soil-related parameters

280 We obtained the Soilgrid v2 data with an original resolution of 250 m (Poggio et al., 2021) to
281 prepare soil properties. Soilgrid is generated using machine learning based on multiple data
282 sources of soil profiles and remote sensing data (Hengl et al., 2017). The soil product underwent
283 rigorous quantitative evaluation using a cross-validation method, which ensures alignment with
284 established pedo-landscape features and provides spatial uncertainty to guide product users
285 (Poggio et al., 2021). Soilgrid v2 provides percent clay, percent sand, and soil organic matter for
286 six standard soil layers: 0–5 cm, 5–15 cm, 15–30 cm, 30–60 cm, 60–100 cm, and 100–200 cm.
287 The original SoilGrid version 2 data obtained from GEE were processed at 1 km resolution with
288 multiple layers using an area-weighted average method. To facilitate the demonstration, we
289 restructured the six soil layers vertically into ELM2's ten effective soil layers (0–1.8 cm, 1.8–4.5
290 cm, 4.5–9.1 cm, 9.1–16.6 cm, 16.6–28.9 cm, 28.9–49.3 cm, 49.3–82.9 cm, 82.9–138.3 cm, 138.3–
291 229.6 cm, and 229.6–380.2 cm) using the nearest neighboring method. It should be noted that the
292 lake module in ELM2 and CLM5 requires soil properties, but the Soilgrid v2 data may not provide

Deleted: ELM's

Formatted: Font color: Text 1

Formatted: Font color: Text 1

Deleted: ELM's

298 coverage over water surfaces. To address this, we utilized the nearest neighbor sampling method
299 to map the 1 km soil properties onto the terrestrial water surface.

300

301 2.4 Topography-related parameters

302 ~~We employed the~~ digital elevation from ~~the Multi-Error-Removed Improved-Terrain DEM~~
303 ~~(MERIT DEM, Yamazaki et al., 2019) to obtain~~ topography-related parameters. ~~The MERIT DEM~~
304 ~~provides globally consistent elevation data at 90 m resolution, distinguished by its exceptional~~
305 ~~vertical accuracy. This accuracy was rigorously validated against ICESat's lowest elevations in~~
306 ~~both forested and non-forested regions and was further benchmarked using the UK's premium~~
307 ~~airborne LiDAR DEM (Yamazaki et al., 2019).~~ We first acquired the 1km elevation and standard
308 deviation of elevation using GEE based on the original 90 m elevation. Further, we calculated the
309 slope, aspect, sky view factor, and terrain configuration factor from the 1km elevation using the
310 parallel computing tool developed by Dozier (2022). The sky view factor represents the proportion
311 of visible sky limited by adjacent terrain, and the terrain configuration factor describes the
312 proportion of adjacent terrain which is visible to the ground target. Finally, to drive the
313 parameterization of sub-grid topographical effects on solar radiation (Hao et al., 2022) in ELM2,
314 we calculated the $\sin(\text{slope}) \cdot \sin(\text{aspect})$ and $\sin(\text{slope}) \cdot \cos(\text{aspect})$ for calculating the
315 local solar incident angle, and two normalized angle-related factors, the sky view factor, and terrain
316 configuration factor by $\cos(\text{slope})$. ~~It is important to note that the standard deviation of elevation~~
317 ~~calculated in this study is specific to the 1 km resolution simulation. For applications requiring~~
318 ~~coarser resolutions (e.g., 0.5 degree), the standard deviation should be recalculated directly from~~
319 ~~the 1 km elevation, rather than averaging from the 1k standard deviation of elevation.~~

320

Deleted: The 90 m

Deleted: Hydro (

Deleted: was used

Deleted: derive

Formatted: Font color: Text 1

Deleted: ¶

2.5 Comparison between new and existing land surface parameters

In this study, since the data sources used to develop the 1k global land surface parameters have already undergone rigorous validation, we do not perform additional evaluations against reference datasets (e.g., observations). Instead, our focus is on comparing the newly developed 1k parameters with those from K2012 and the ELM2/CLM5 default parameters. The K2012 parameters, obtained through personal communication (refer to the data availability section for details). The ELM2/CLM5 default parameters were sourced from the CESM input data repository (<https://svn-ccsm-inputdata.cgd.ucar.edu/trunk/inputdata/>). Given the different resolutions of these datasets—our new parameters at 1km, K2012 at 0.05 degree, and ELM2/CLM5 defaults with varying resolutions—we adapt our comparison at different resolutions for different variables.

For PFT parameters, we aggregated both the 1k new parameters and the 0.05-degree K2012 data to the 0.5-degree resolution of the ELM2/CLM5 default. For non-vegetated land units (i.e., urban, glacier, and lake), we upscaled the 1k new parameters to a 0.05-degree resolution to align with the ELM2/CLM5 default. It is important to note that the urban parameter in K2012 is only available for the northern hemisphere, due to limitations in data acquisition.

When comparing LAI, we aggregated the 1k new and K2012 LAI to 0.5-degree resolution, matching the ELM2/CLM5 default LAI/SAI resolution. We excluded the comparison of SAI from our analysis due to the limited availability of the global K2012 dataset, from which we only acquired coverage for North America. We have not included a comparison of vegetation canopy height (top and bottom parameters) in our study. This is because the K2012 dataset does not contain these parameters, and the ELM2/CLM5 default parameters in the CESM input data repository provide only tabular values for each PFT, rather than spatially variable canopy heights for tree PFTs.

349 For soil and topography-related parameters, our comparison was limited to the 1k new parameters
350 and the ELM2/CLM5 default, as K2012 does not include these parameters. Specifically, for soil
351 comparisons, we aggregated the new 1k parameters to 0.083° resolution to match the ELM2/CLM5
352 default soil parameters. For topography, given that the ELM2/CLM5 default parameters is a
353 combination of 1k and 10 arc-minute data sources, we simplify the comparison by aggregating
354 both the new 1k parameters and ELM2/CLM5 default to 0.5-degree resolution, including elevation
355 and slope.

356

357 3. K-scale demonstration simulation over CONUS

358 3.1 Experiment design

359 To demonstrate the capability of 1 km datasets, we conducted ELM2 simulations over CONUS at
360 the resolution of 1 km, using the newly developed 1 km land surface parameters for 2010. We used
361 atmospheric forcing from the Global Soil Wetness Project Phase 3 (GSWP3; Kim, 2017) with a
362 spatial resolution of 0.5° to drive ELM. The spatial homogeneity of atmospheric forcings within
363 0.5° grid cell guarantees that the spatial variability of ELM simulated variables (e.g., latent heat)
364 within 0.5° grid cell is solely attributable to the heterogeneity of the 1 km land surface parameters.
365 There are approximately 12 million effective grids over CONUS. We ran ELM for five years
366 (2010–2014), and the last year's simulation was used for analysis. We specifically analyzed the
367 annual mean of surface layer soil moisture (SM, m^3/m^3), latent heat (LH, W/m^2), emitted
368 longwave radiation (ELR, W/m^2), and absorbed shortwave radiation (ASR, W/m^2).

Deleted: forcing

Deleted: year's

369 3.2 Spatial scaling analysis

370 We conducted a spatial scaling analysis following the method described in Vergopolan (2022) on
371 the 1 km ELM simulation data to better understand how k-scale spatial heterogeneity in the four
372 ELM-simulated variables (mentioned in Section 3.1) induced only by spatial heterogeneity of land
373 surface parameters changes across spatial scales. First, we performed upscaling by averaging the
374 1 km ($=1/120^\circ$) land surface parameters and the four ELM-simulated variables to coarser spatial
375 scales, λ_{scale} of $1/60^\circ$, $1/40^\circ$, $1/30^\circ$, $1/24^\circ$, $1/20^\circ$, and $1/10^\circ$, and calculated the spatial standard
376 deviation (σ_{scale}) within each $0.5^\circ \times 0.5^\circ$ box at each spatial scale (Table 2). Second, we quantified
377 the changes in spatial variability at different spatial scales compared to the original 1km resolution
378 by calculating the ratio of σ_{scale} to $\sigma_{1 km}$. Third, we fitted a $\log\left(\frac{\sigma_{scale}}{\sigma_{1 km}}\right) \propto \beta \times \log\left(\frac{\lambda_{scale}}{\lambda_{1 km}}\right)$
379 relationship, where β is an indicator to quantify data spatial variability persistence across scales

382 (Hu et al., 1997). A more negative β indicates a larger dependency of data spatial variability on
 383 spatial scales, resulting in a higher information loss, denoted as $\gamma_{scale} = (1 - \sigma_{scale} / \sigma_{1\text{ km}}) \times$
 384 100% . In this study, we focus on information loss at a 12 km scale, denoted as $\gamma_{12\text{ km}}$. For
 385 simplicity in subsequent discussion, $\gamma_{12\text{ km}}$ will be referred to as γ in the results section. Given the
 386 possibility that β may not demonstrate significant temporal variation (Mälicke et al., 2020), and
 387 considering that our scaling analysis is intended for demonstration purposes, our spatial scaling
 388 analysis is based on the annual mean of ELM2 simulations.

Deleted: $\gamma = (1 - \sigma_{scale} / \sigma_{1\text{ km}}) \times 100\%$.

389 Table 2. Spatial resolution and pixel number at different spatial scales.

$\lambda_{scale} / \lambda_{1\text{ km}}$	1	2	3	4	5	6	12
Spatial resolution	1km (1/120°)	2km (1/60°)	3km (1/40°)	4km (1/30°)	5km (1/24°)	6km (1/20°)	12km (1/10°)
Pixel number within 0.5° × 0.5° box	60 × 60	30 × 30	20 × 20	15 × 15	12 × 12	10 × 10	5 × 5

Deleted: λ_{scale}

390

391 3.3 Attribution analysis utilizing XML methods

392 We conducted additional analysis to determine the primary land surface parameters that influence
 393 the spatial scaling of ELM simulations. We employed XML methods, specifically the eXtreme
 394 Gradient Boosting(XGBoost; Chen and Guestrin, 2016) machine learning algorithm and the game
 395 theoretic approach SHapley Additive exPlanations (SHAP; Lundberg and Lee, 2017; Lundberg et
 396 al., 2018, 2020). XML methods were utilized to assess the influence of land surface parameters on
 397 the spatial variability and information loss of ELM2 simulations across the CONUS. Taking spatial
 398 variability as an example, we first computed the standard deviation (σ) within each 0.5° x 0.5° grid
 399 for both 1 km resolution land surface parameters and simulations. Then, we train a machine
 400 learning model to predict the spatial variability of each simulated variable (i.e., SM, LH, ELR,
 401 ASR). We used the spatial variability (i.e., σ) and mean (μ) of the land surface parameters and μ

404 of precipitation and temperature as predictor variables, and the simulated variable's σ as the target
405 variable. After training the machine learning model, we used SHAP to quantify the relative
406 importance and determine which factors were most important in driving the spatial variability of
407 the simulations. Similarly, we used this approach to identify the most critical drivers of information
408 loss.

409

410 **3. Results**

411 **3.1 Demonstration of the global 1km land surface parameters**

412 LAI generally shows high values in humid and warm regions, such as tropical rainforests,
413 southeastern US, and southern Asia, and low values over arid or cold regions, such as central
414 Australia, southwestern US, Middle East, Central Asia, and northern Canada (Figure 1a). At high
415 resolution, the LAI dataset clearly reflects the detailed heterogeneity of vegetation distributions.
416 In subregion R1 (Figure 1b), a relatively small LAI is distributed over mountain ridges and zero
417 LAI over water surfaces (e.g., lakes). In subregion R2 (Figure 1c), the LAI pattern shows a large
418 proportion of forest fragmentation caused by deforestation. In subregion R3 (Figure 1d), the LAI
419 shows the distribution of agricultural land along with the river, river mouth, and lakes under an
420 arid climate. R4 shows how urbanization affects vegetation distributions (Figure 1e).

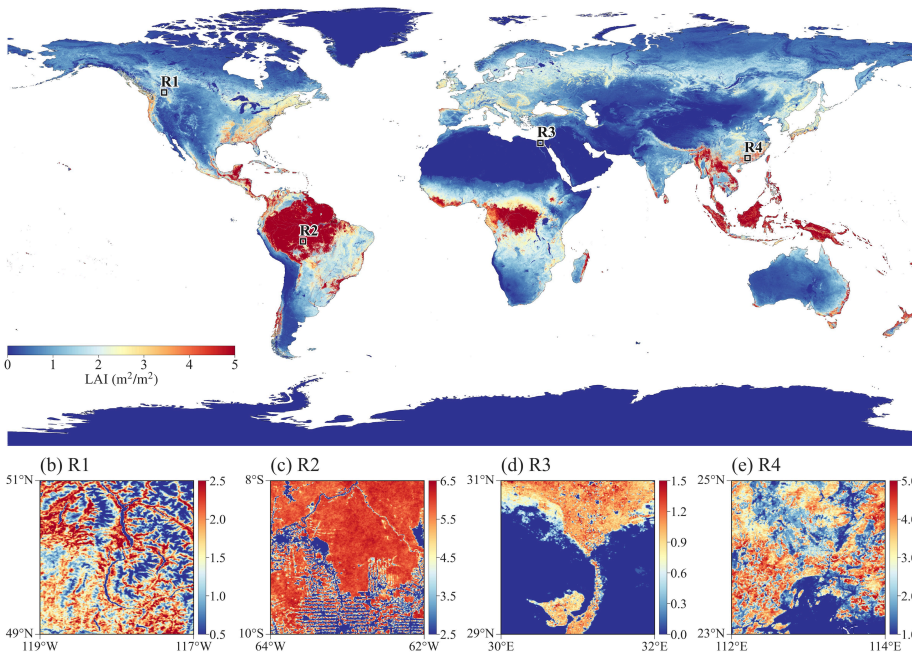
421 Figure 2 demonstrates the distribution of plant functional types and other non-vegetation land units.

422 High-resolution LULC types over multiple years can benefit studies related to LULC changes like
423 urbanization and deforestation. Canopy height generally follows a similar spatial pattern with LAI,
424 with high values in humid and warm regions and low values over arid or cold regions (Figure 3a).

425 The percent clay shows high values over Southeast Asia, India, central Africa, and southeast South
426 America, and low content over North Europe, South Africa and Alaska (Figure 3b). The

427 topography factors follow the elevation patterns (Figures 3c and 3d), where there are large slopes
 428 and standard deviation of elevation over mountainous regions, such as the Rocky Mountains in
 429 North America, the Himalayas Mountains in Asia, and Andes Mountains in South America.

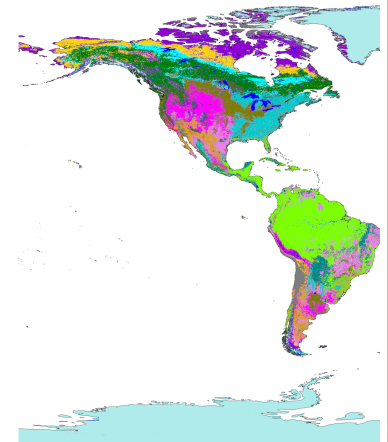
(a) LAI (m²/m²)



430
 431 Figure 1. The spatial pattern of LAI (annual mean in 2010) over (a) global land and (b)~(e) four
 432 subregions R1~R4 within 2-degree boxes marked in (a). Subregions R1~R4 represent
 433 topography, deforestation, irrigations, and urbanization effects on LAI.

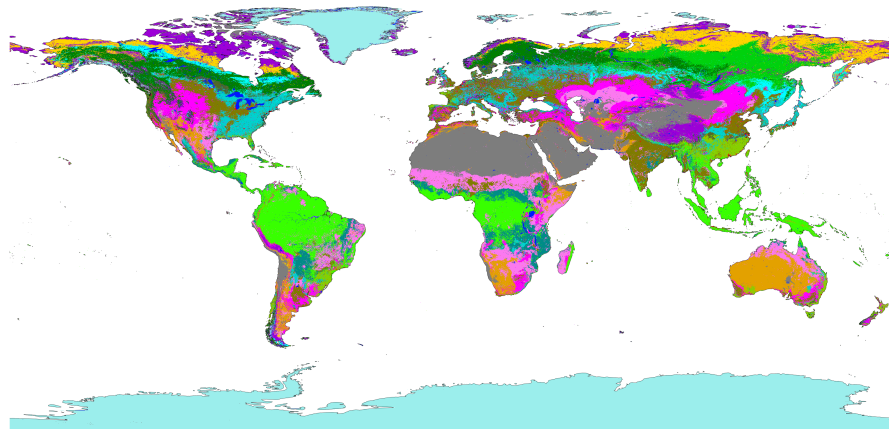
434

Deleted:Page Break.....



- Bare soil
- Needleleaf evergreen tree, temperate
- Needleleaf evergreen tree, boreal
- Needleleaf deciduous tree
- Broadleaf evergreen tree, tropical
- Broadleaf evergreen tree, temperate
- Broadleaf deciduous tree, tropical
- Broadleaf deciduous tree, temperate
- Broadleaf deciduous tree, boreal
- Broadleaf evergreen shrub, temperate

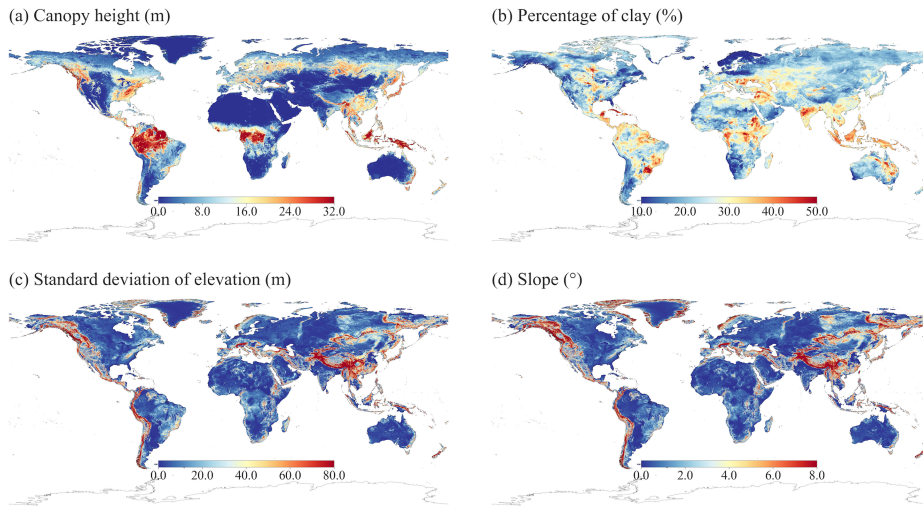
Deleted:
 Figure 2. Global LULC distribution in year 2010.



- | | | |
|-----------------|-----------------|-----------|
| ■ Bare Soil | ■ BDT-Temperate | ■ C3G |
| ■ NET-Temperate | ■ BDT-Boreal | ■ C4G |
| ■ NET-Boreal | ■ BES-Temperate | ■ Crop |
| ■ NDT-Boreal | ■ BDS-Temperate | ■ Lake |
| ■ BET-Tropical | ■ BDS-Boreal | ■ Glacier |
| ■ BET-Temperate | ■ C3G-Arctic | ■ Urban |
| ■ BDT-Tropical | | |

439

440 Figure 2. Global LULC distribution in year 2010. PFT abbreviations include: Bare Soil, Needleleaf
 441 Evergreen Trees in temperate (NET-Temperate) and boreal (NET-Boreal) regions, Needleleaf
 442 Deciduous Trees in boreal regions (NDT-Boreal), Broadleaf Evergreen Trees in tropical (BET-
 443 Tropical) and temperate (BET-Temperate) regions, Broadleaf Deciduous Trees in tropical (BDT-
 444 Tropical), temperate (BDT-Temperate), and boreal (BDT-Boreal) regions, Broadleaf Evergreen
 445 Shrubs in temperate regions (BES-Temperate), Deciduous Shrubs in temperate (BDS-Temperate)
 446 and boreal (BDS-Boreal) regions, C3 Grass in arctic (C3G-Arctic) and general (C3G) varieties,
 447 C4 Grass (C4G), Crop, Lake, Glacier, and Urban.



448
 449 Figure 3. Demonstration of global 1km datasets (a) Canopy top height, (b) percent clay, (c)
 450 standard deviation of elevation, and (d) slope.

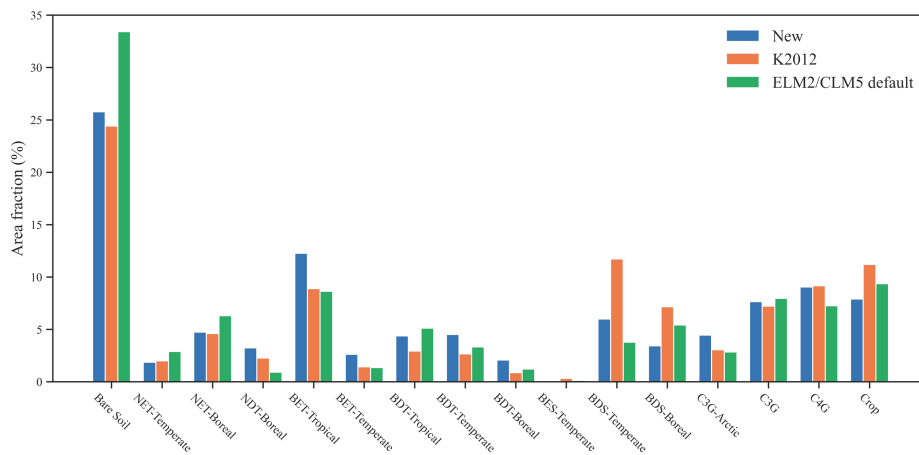
451

452 **3.2 Comparison between new and existing land surface parameters**

Deleted: 3.2

453 The global distributions of different PFTs show varying degrees of difference when comparing the
 454 new parameters with the K2012 and ELM2/CLM5 default parameters (Figure 4 and
 455 Supplementary Figures S1 to S16). Predominant types such as bare soil, BET-Tropical tree, C3
 456 and C4 grass, and crop are found consistently across all datasets. Notable differences include less
 457 bare soil in the new parameters and K2012 compared to ELM2/CLM5 default, especially in high-
 458 latitude North America, western US, South Africa, Central Asia, and Central Australia (Figure S1).
 459 While the new NDT PFT shows larger coverage in Siberia than K2012 and ELM2/CLM5 (Figure
 460 S4), BET-Tropical PFT is more prevalent in the new parameters across Central and South America
 461 (Figure S5). BET-Temperate PFT has greater area coverage in southern China in the new
 462 parameters (Figure S6). For BDT-Tropical, BDT-Temperate, and BDT-Boreal PFTs, both the new

464 and ELM2/CLM5 default parameters surpass K2012 data in coverage (Figures S7 to S9). The
 465 coverage of new BDS-Temperate PFT is smaller than K2012 but larger than ELM2/CLM5 default
 466 (Figure S11), and the new BDS-Boreal PFT is less extensive in the boreal northern hemisphere
 467 compared to both K2012 and ELM2/CLM5 defaults (Figure S12). The C3-Arctic PFT shows
 468 larger areas in the new parameters, particularly in northern Canada, with the new C4 grass PFT
 469 being similar to that of K2012 and larger than ELM2/CLM5 C4 grass. Crop PFT is less extensive
 470 in the new parameters, particularly in Southeastern China, Europe, South America, Africa, and
 471 Australia.

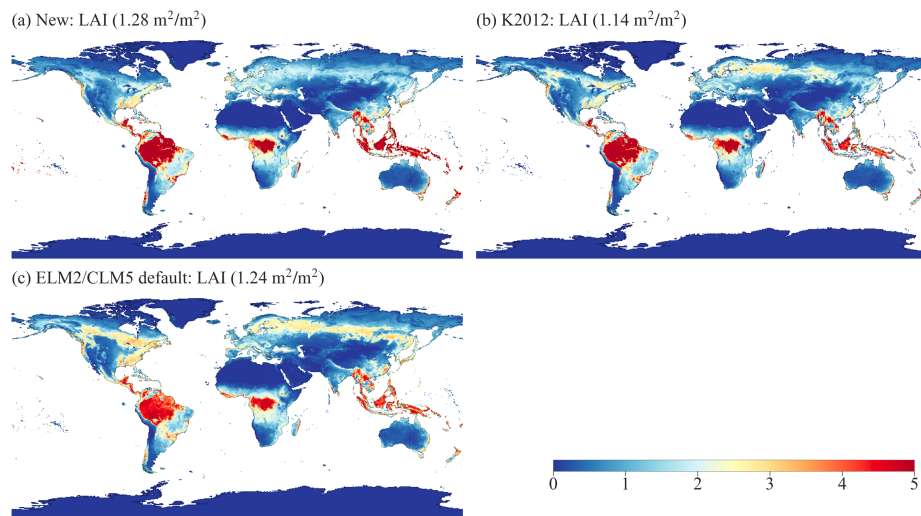


472 Figure 4. The global average area fractions of PFTs for three land surface parameter datasets. PFT
 473 abbreviations used on the X-axis are displayed in Figure 2.

475 The global distributions of non-vegetated land covers of lake, glacier and urban areas vary among
 476 the datasets (Figure S17–S19). The new dataset shows slightly less lake coverage than K2012, but
 477 both are smaller than ELM2/CLM5 default, particularly in high-latitude North America (Figure
 478 S17). Glacier coverage in the new parameter is around 0.7% smaller than K2012, with noticeable
 479 S17).

480 differences in the Arctic North America, while ELM2/CLM5 default shows more extensive glacier
481 coverage in Antarctica (Figure S18). Regarding urban areas, K2012 has the smallest urban
482 coverage in the Northern Hemisphere compared to both the new dataset and ELM2/CLM5 default
483 (Figure S19). Meanwhile, ELM2/CLM5 default exhibits more expansive urban areas in India and
484 China than the new dataset and K2012.

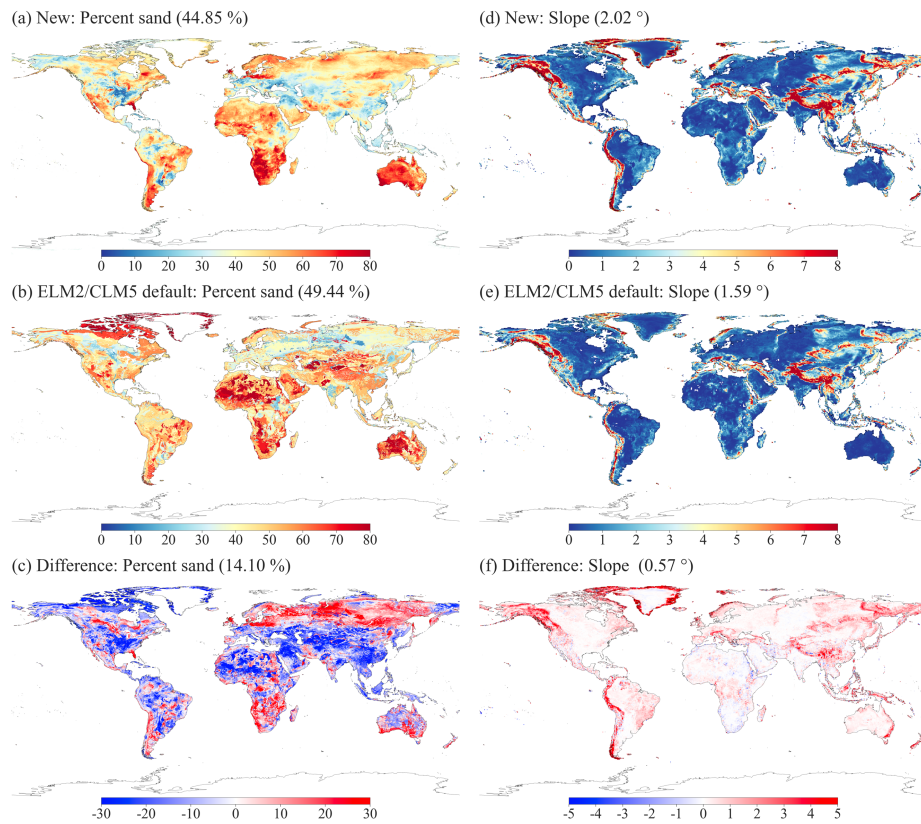
485
486 The global annual mean LAI exhibits similar spatial patterns among the new parameter, K2012,
487 and ELM2/CLM5 (Figure 5). The overall global mean LAI for the new parameter (1.28 m²/m²) is
488 slightly higher than that of K2012 (1.14 m²/m²) and the ELM2/CLM5 default data (1.24 m²/m²).
489 In terms of spatial pattern, the new LAI, relative to K2012 (Figure S20a), shows lower values in
490 the NET-Boreal PFT over the northern hemisphere, but higher values in the BET-Tropical PFT
491 over the tropics. Similarly, compared with the ELM2/CLM5 default LAI (Figure S20b), the new
492 LAI also presents smaller values in both the NET-Boreal and NDT PFTs over the northern
493 hemisphere, but larger values in the BET-Tropical PFT regions.



494
 495 Figure 5. Comparison of global annual mean LAI for (a) new, (b) K2012, and (c) ELM2/CLM5
 496 default parameters. The global average is indicated in the subplot title.

497
 498 Soil parameters exhibit significant differences between the new and ELM2/CLM5 default datasets
 499 (Figures 6a-bc, S21, and S22). The global mean absolute differences between the new and
 500 ELM2/CLM5 default for percent sand, percent clay, and organic matter are 14.1%, 8.1%, and 30.5
 501 kg/m³, respectively. Generally, the new soil parameters are spatially distributed more smoothly
 502 than those from ELM2/CLM5 with more patchy patterns (Figure 6a vs. 6b). Specifically, the new
 503 percent sand is higher in regions like Europe, Siberia, South Africa, and Southern Australia, but
 504 lower in areas such as the Lower Mississippi River Basin, North Africa, and Central and
 505 Southeastern Asia (Figure 6c). The new percent clay shows larger values in the Western US, North
 506 Africa, Central Asia, and Australia, but smaller values in Alaska and Eastern Europe (Figure S21).

507 For organic matter, the new parameter indicates smaller values in the Northern Hemisphere but
508 larger values in other global regions compared to the ELM2/CLM5 default (Figure S22).
509 Topography-related parameters exhibit broadly similar spatial patterns but with notable
510 differences between the new and ELM2/CLM5 default parameters, as seen in Figures 6d-6f and
511 S23. The new slope parameter generally shows a larger slope relative to the ELM2/CLM5 default,
512 particularly in mountainous regions (Figure 6f). This could be attributed to the new 1 km slope
513 being calculated from a finer 90 m resolution elevation. Differences in elevation between the new
514 and ELM2/CLM5 parameters are more pronounced in areas such as various mountainous regions,
515 Greenland, the Amazon Basin, the Tibetan Plateau, and Australia (Figure S23).



516
 517 Figure 6. Comparisons of percent sand and slope. (a) new and (b) ELM2/CLM5 default percent
 518 sand, along with (c) their difference (new – ELM2/CLM5 default) for percent sand; (d) new, (e)
 519 ELM2/CLM5 default, and (f) their difference for slope. The global average is shown in the subplot
 520 titles, with the global average of the absolute difference provided for (c) and (f).

521
 522 **3.3 Demonstration 1km simulation over CONUS**
 523 ELM simulations at a 1 km resolution display significant spatial heterogeneity over CONUS
 524 (Figure 7). The values of SM, LH, ELR, and ASR across CONUS follow approximately normal

Deleted: 4

526 distributions, with averages of $0.3 \text{ m}^3/\text{m}^3$, $39.0 \text{ W}/\text{m}^2$, $371.7 \text{ W}/\text{m}^2$, $156.7 \text{ W}/\text{m}^2$, respectively (as
 527 shown in the histogram plots in Figure 7). SM shows drier conditions over the West and Southwest
 528 and wetter conditions over the Midwest, Corn Belt, Mississippi River basin, and Northeast (Figure
 529 7a). LH shows high values over the central and southeast, and lower values over the west and
 530 southwest (Figure 7b). The ELR generally shows higher values over regions with high surface
 531 temperature in the south (Figure 7c). The ASR shows higher values over the southwestern regions
 532 determined by incoming solar radiation and albedo (Figure 7d). Despite the high-resolution
 533 heterogeneity shown at 1 km resolution, we can still see the spatial patterns distinguished at coarse
 534 resolution, i.e., $0.5^\circ \times 0.5^\circ$. These coarser footprints are from the GSWP3 atmospheric forcing with
 535 0.5° resolution. As concluded by Li et al. (2022), atmospheric forcing is one primary heterogeneity
 536 source for land surface modeling. Therefore, k-scale atmospheric forcing needs to be developed to
 537 further advance k-scale offline land surface modeling.

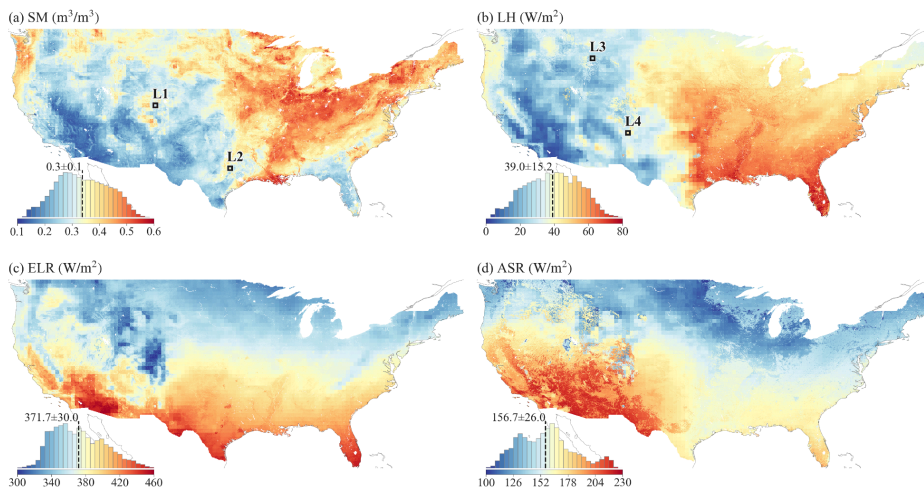
Deleted: 4

Deleted: 4a

Deleted: 4b

Deleted: 4c

Deleted: 4d



538
 539 Figure 7. The annual mean of 1 km simulations of (a) SM, (b) LH, (c) ELR, and (ASR) over
 540 CONUS. The $0.5^\circ \times 0.5^\circ$ boxes marked as L1, L2, L3, and L4 in (a) and (b) are selected to

Deleted: 4

547 demonstrate the spatial scaling analysis. The inserted histogram plot illustrates the distribution of
548 ELM2 simulations.

549

550 **3.4 Demonstration of spatial scaling across scales**

551 We next demonstrate the relationships between spatial variabilities and spatial scales for SM and
552 LH. Four locations (in Figures 4a and 4b) are specifically chosen to showcase varying levels of
553 spatial information loss: L1 and L3 demonstrate a relatively large loss for SM and LH, respectively,
554 while L2 and L4 represent a relatively small loss for SM and LH, respectively.

555 At location L1 (Figure 8a), when the 1 km simulation is upscaled to coarser resolutions (i.e., larger
556 spatial scale ratios), the spatial variability of SM decreases, resulting in a negative slope of β . As

557 shown in Figure 9a, compared to the original 1 km resolution, the information loss γ reaches up to
558 54.9% at the 12 km spatial scale. The spatial pattern of SM is consistent with the spatial pattern of
559 percent clay (Figures 6a vs. 6b and 6c vs. 6d), indicating that soil texture contributes significantly
560 to the spatial variability of SM. However, SM has a more negative β than the percent clay ($\beta = -$

561 0.28 vs. -0.19 at L1, as shown in Figure 8a), suggesting that SM variability is amplified likely by
562 other processes that are also influenced by soil texture. In contrast to location L1, location L2
563 exhibits less negative β values for both SM and percent clay, suggesting that their spatial
564 variabilities exhibit less scale dependence (Figures 5a, 6c, and 6d). Both SM and percent clay at
565 location L2 approximately maintain their spatial patterns of high values in the west and low values
566 in the east across spatial scales (Figures 6c and 6d).

567 For LH, there is a more negative β value at location L3 than at location L4 ($\beta = -0.27$ at L3 vs. $-$
568 0.08 at L4, as shown in Figure 8b), which indicates a larger decrease of spatial variability across
569 spatial scales and lower variability persistence at location L3 than location L4 (Figure 10). The

Deleted: 3

Deleted: 5a

Deleted: 6a

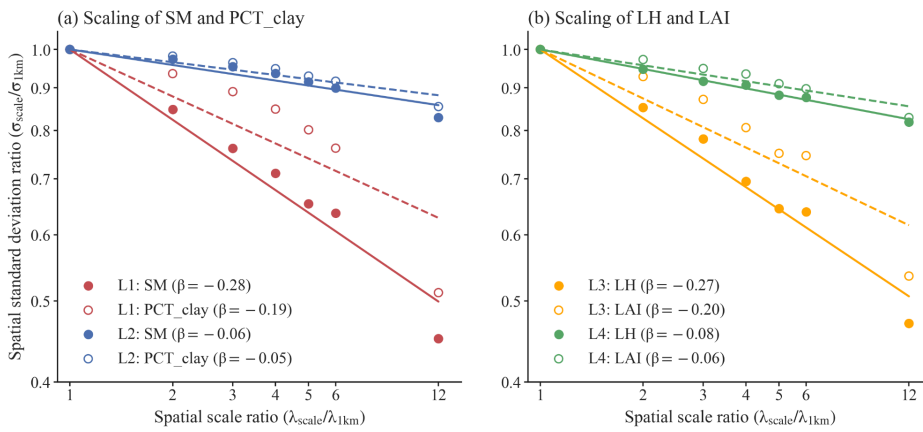
Deleted: 5a

Deleted: 5b

Deleted: 7

576 spatial pattern of LH is consistent with the spatial pattern of LAI (Figures 7a vs. 7b and 7c vs. 7d)
 577 at different spatial scales, suggesting that vegetation plays a significant role in the spatial
 578 variability of LH. Similar to comparison between SM and soil texture, LH has a more negative β
 579 than LAI (Figure 8b).

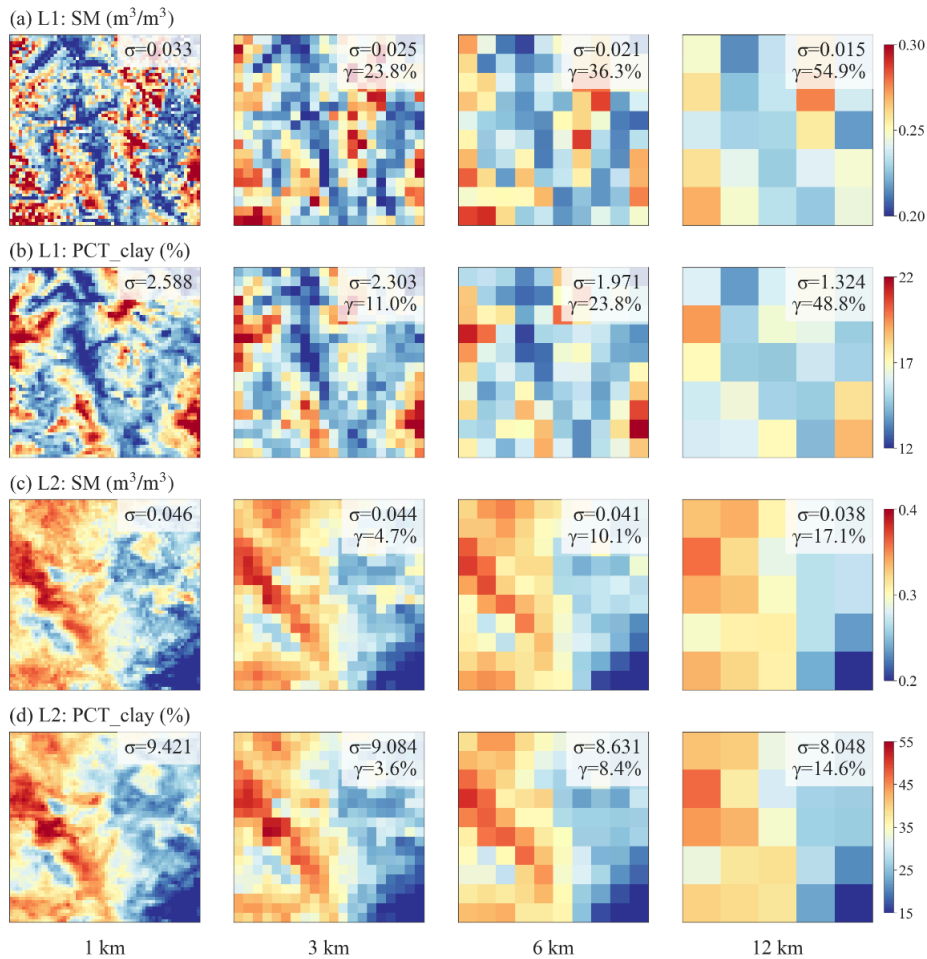
Deleted: 5b



580 Figure 8. The scaling of spatial variabilities for (a) SM and percent clay, and (b) LH and LAI. Both
 581 the x-axis and y-axis are in logarithmic scale. The slope of the linear regression line, β , quantifies
 582 the strength of the negative relationship between spatial scale and spatial variability. A more
 583 negative β value indicates a higher spatial-scale dependency and increased information loss at
 584 coarser spatial scales. Four $0.5^\circ \times 0.5^\circ$ boxes (displayed in Figure 7), namely L1 to L4, are chosen
 585 to contrast larger and smaller negative β values for SM and percent clay (L1 and L2) and for LH
 586 and LAI (L3 and L4).
 587

Deleted: 5

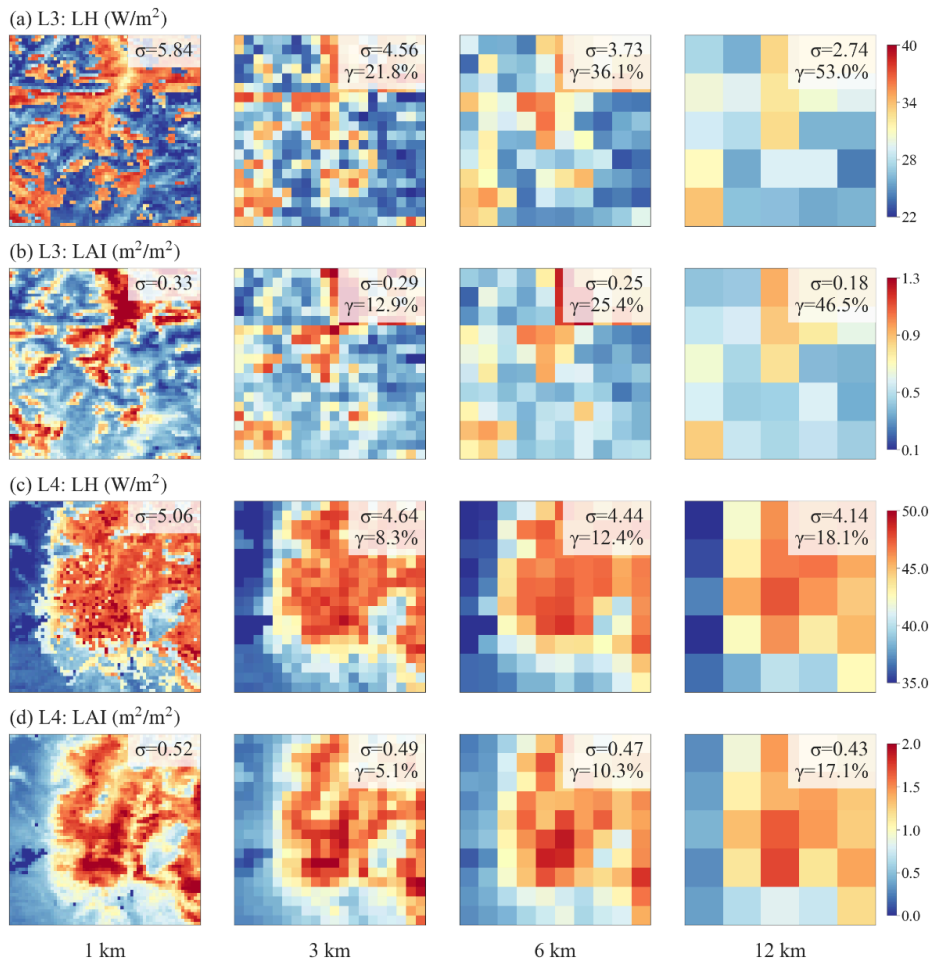
Deleted: 4



591
 592 Figure 9. Comparison of SM and percent clay across spatial scales at locations L1 and L2
 593 highlighted in Figure 7. Each subplot displays the spatial patterns of SM or percent clay within a
 594 $0.5^\circ \times 0.5^\circ$ box, with the σ and γ presented in the legend.

Deleted: 6

Deleted: 5



597

598 Figure 10. Similar to Figure 9, but for LH and LAI at locations L3 and L4.

Deleted: 7

Deleted: 6

601 **3.5 The spatial variability of water and energy simulations and their drivers**

602 We quantified the spatial variability simulated at 1 km resolution using σ within each $0.5^\circ \times 0.5^\circ$
603 box across CONUS. Four ML models were built to explore the spatial relationships between σ and
604 its potential drivers including σ of the land surface parameters and the temperature and
605 precipitation averaged over the grid box. Overall, the ML models performed well in predicting the
606 σ of the simulated variables, with small root mean square error (RMSE) and large R^2 (see Figure
607 [S24](#)). SM shows larger spatial variability in the US Southern Coastal Plain, lower Mississippi
608 River, Northeast, Southeast, and regions around the Great Lake (Figure [11a](#)), which is roughly
609 consistent with the spatial heterogeneity of the high-resolution SM simulation in Vergopolan et al.
610 (2022). Based on the SHAP method, the spatial variability of SM across CONUS is driven by
611 various factors, mainly including the spatial variabilities of percent sand and percent clay, mean
612 precipitation, the σ and μ of soil organic matter, the σ of canopy height, and mean temperature
613 (Figure [11b](#)). Mean precipitation and temperature reflect climate conditions (Figure [S26](#)), which
614 are related to the water supply and water demand of soil water content. The spatial heterogeneity
615 of soil properties, such as texture and organic matter content, affects soil hydraulic properties and
616 generate more spatially variable soil water content. Vegetation characteristics, such as canopy
617 height and LAI, could influence SM spatial variability through their effect on roughness length
618 and rooting depth.

619 The spatial variability of LH is large in the southeastern, central, and western mountainous regions
620 of the US (Figure [11c](#)). Vegetation properties and climate conditions mainly drive the variability
621 of LH (Figure [11d](#)). The μ and σ of LAI can affect transpiration and soil evaporation, while canopy
622 height can influence surface roughness length and, in turn, evapotranspiration. Mean precipitation

Deleted: 4

Deleted: S1

Deleted: 8a

Deleted: 8b

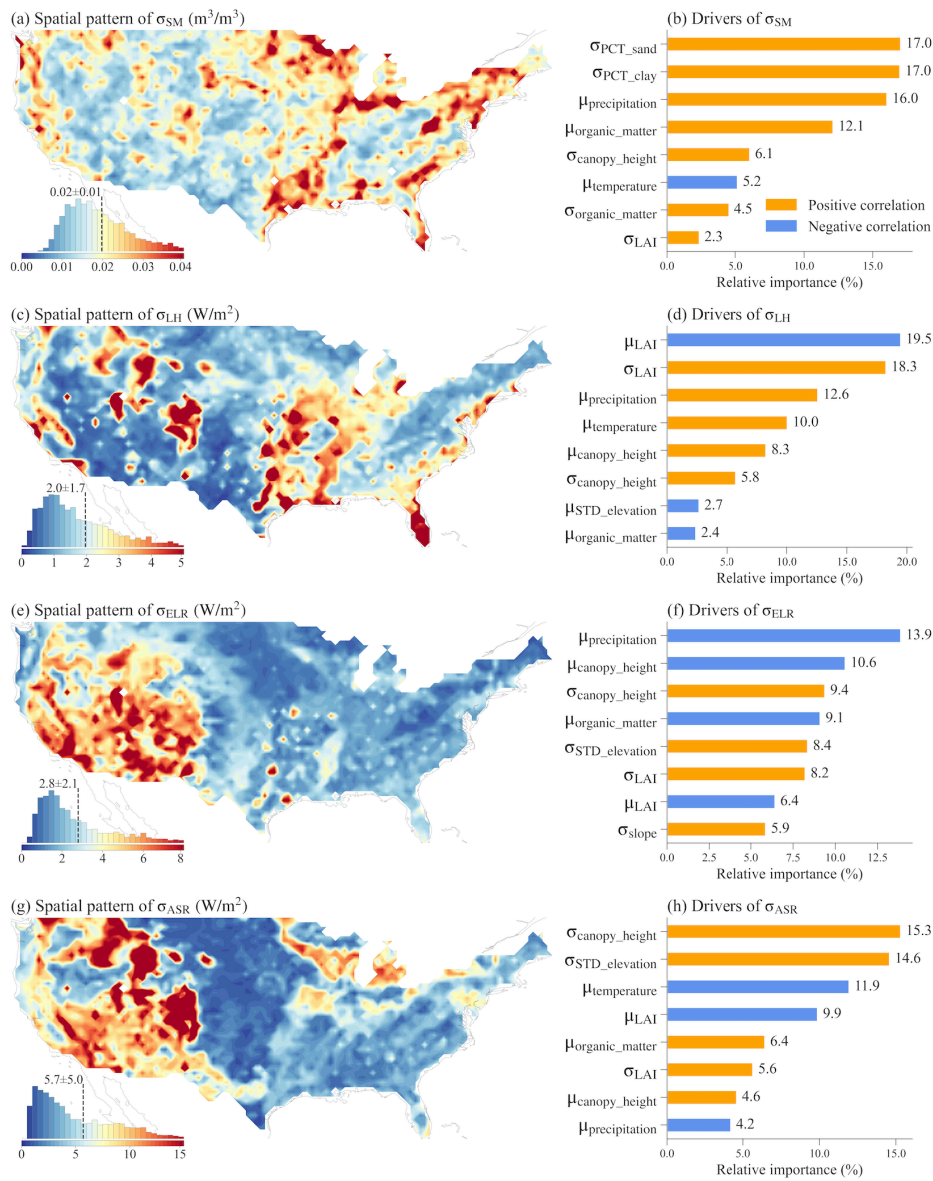
Deleted: S3

Deleted: 8c

Deleted: 8d

630 and temperature reflect the overall climate conditions related to the water and energy available for
631 latent heat.

632 ELR and ASR exhibit large spatial variability mainly over the western US, with ASR additionally
633 showing significant spatial variability across the Northern US (Figures 8e and 8g). This variability
634 is primarily driven by climate conditions such as mean precipitation and temperature, topographic
635 features such as standard deviation of elevation and slope, and vegetation properties including LAI
636 and canopy height (Figures 8f and 8h). These factors are related to the radiation input and surface
637 properties, such as albedo and roughness length, which impact the energy cycles and availability
638 of ELR and ASR.



639
 640 Figure 11. The spatial variability over each $0.5^\circ \times 0.5^\circ$ grid cell (left plots) and the top eight most
 641 important drivers (right plots) of the spatial variability for SM, LH, ELR, and ASR. The inserted

Deleted: 8

643 histogram plot illustrates the probability distribution of the spatial variability across CONUS. The
644 relative importance of each variable in determining the spatial variability is calculated as the ratio
645 of the mean |SHAP value| of the variable to the sum of the mean |SHAP value| of all variables.
646 Therefore, the sum of the relative importance of all variables is 100%.

647

648 **3.6 The information loss of water and energy simulations and their drivers**

649 We also evaluated the information loss in simulations when upscaling from 1 km to 12 km
650 resolution and analyzed the drivers of their spatial patterns over CONUS. Four ML models were
651 built to explore the relationships between the γ of the simulations and its drivers including the γ of
652 the land surface parameters and the mean temperature and precipitation averaged over the $0.5^\circ \times$
653 0.5° box. These ML models performed well in predicting the simulations' γ , with small RMSE and
654 large R^2 (Figure S25).

655 Significant information loss ranging from 31% to 54% with maximum values exceeding 90% is
656 observed for SM, LH, ELR, and ASR simulations (Figure 12). Their spatial patterns and drivers
657 show distinct variations. γ_{SM} is primarily driven by the information loss of percent clay and sand,
658 mean soil organic matter, and mean temperature, which affects the soil hydraulic properties and
659 soil water balance (Figures 9a and 9b). γ_{LH} displays high values in the eastern US and low values
660 in the western US (Figure 12c). It is primarily contributed by the information loss of vegetation
661 properties such as LAI and canopy height, and mean LAI, which influences the partitioning of LH
662 and sensible heat, and the partitioning of transpiration and evaporation (Figure 12d). γ_{ELR} exhibits
663 high values in the central and eastern US, particularly in the northeastern US, while γ_{ASR} has high
664 values almost all over the US, especially in the eastern regions (Figures 9e and 9g). γ_{ELR} and γ_{ASR}
665 are largely driven by vegetation properties such as LAI and canopy height, which are associated

Deleted: 5

Deleted: γ

Deleted: γ

Deleted: S2

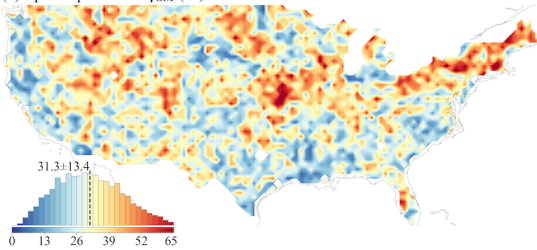
Deleted: 9

Deleted: 9c

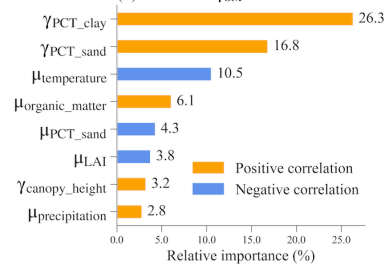
Deleted: 9d

673 with energy processes such as albedo (Figures 9f and 9h). Additionally, topography factors of
674 standard deviation of elevation and slope also slightly contribute to γ_{ASR} .

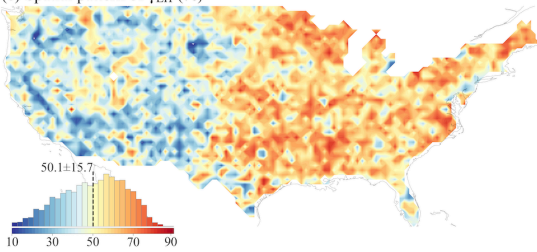
(a) Spatial pattern of γ_{SM} (%)



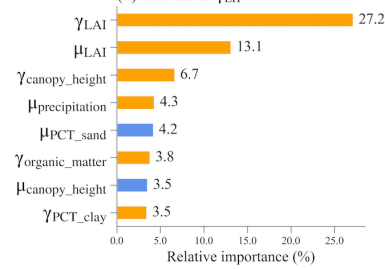
(b) Drivers of γ_{SM}



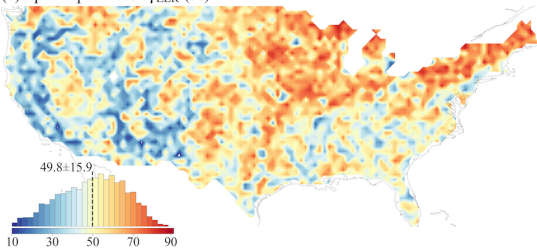
(c) Spatial pattern of γ_{LH} (%)



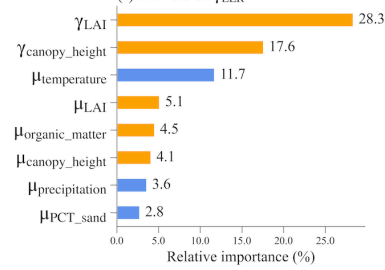
(d) Drivers of γ_{LH}



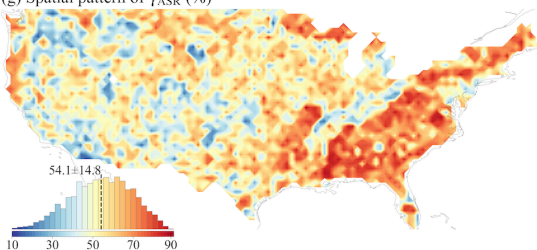
(e) Spatial pattern of γ_{ELR} (%)



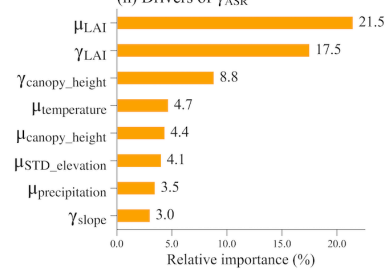
(f) Drivers of γ_{ELR}



(g) Spatial pattern of γ_{ASR} (%)



(h) Drivers of γ_{ASR}



675

676 Figure 12. Same to Figure 11 but for information loss.

Deleted: 9

Deleted: as

Deleted: 8

680 **4. Discussion**

681 The development of new 1 km land surface parameter datasets in this study marks a substantial
682 improvement over commonly used land surface parameters such as CLM5 and K2012, leveraging
683 the latest high-resolution data sources with rigorous validation, including MODIS PFTs, enhanced
684 LAI and canopy height, soil properties, and topography factors. When compared with K2012 and
685 ELM2/CLM5 default datasets, the new 1k parameters exhibit notable differences, suggesting
686 potential improvement due to the use of more advanced data sources. Distinct features of the new
687 parameters include a reduction in bare soil compared to ELM2/CLM5, especially in regions like
688 North America and Central Asia, and diverse coverage of specific PFTs such as NDT and BET-
689 Tropical in areas like Siberia and South America. The LAI of the new parameters diverges from
690 K2012 and ELM2/CLM5, showing lower values in NET-Boreal PFT of the northern hemisphere
691 but higher BET-Tropical PFT in the tropics. The soil parameters, particularly in regions like
692 Europe, Central Asia, and the Western US, show significant differences between the new and
693 ELM2/CLM5 defaults. Moreover, the new parameters indicate larger slopes in mountainous
694 regions and more distinct elevation differences in areas such as Greenland and the Tibetan Plateau
695 compared to ELM2/CLM5. These differences potentially highlight enhanced accuracy and
696 sophistication of the new 1k parameters. Their enhanced resolution and rigorous validation suggest
697 a substantial capacity to improve ESMs modeling. Additionally, the richness of multi-year data
698 for LULC, LAI, and SAI in these datasets is especially valuable for examining land use and cover
699 changes, urbanization trends, deforestation impacts, and agricultural transformations.

700

701 The new 1 km land surface parameters can improve k-scale offline LSMs modeling by better
702 capturing spatial surface heterogeneity. As evidenced by the 1 km ELM simulation over CONUS,

Deleted: The new 1 km land surface parameter datasets developed in this study represent significant improvements over the current datasets. Compared to the two common land surface parameter datasets of CLM5 and K2012, our data are more advanced by utilizing the newest high-resolution data sources, including MODIS PFTs and non-vegetation land units, LAI and SAI, canopy height, soil properties and topography factors. The availability of multi-year data for LULC, LAI, and SAI parameters is advantageous for studies such as LULC changes, including urbanization, deforestation, and agricultural impacts. Incorporating these new 1 km land surface parameters into ESMs will advance the accurate representation and understanding of land surface processes and land-atmosphere interactions. However, certain limitations and opportunities for future development should be noted. The urban extension may differ depending on the data sources, urban definitions, and the algorithms employed, such as those derived from harmonized nighttime lights (Zhao et al., 2022), global artificial impervious area (GAIA, Li et al., 2020b; Gong et al., 2020), urban expansion (Liu et al., 2020; Kuang et al., 2021), which may differ from our urban land units based on MODIS. The urban classification into TBD, HD, and MD in J2010 is based on the global building height. Although there are building height datasets available for specific regions, such as Europe, the US, and China (Yang and Zhao, 2022; Li et al., 2020a; Frantz et al., 2021; Cao and Huang, 2021), a globally consistent building height dataset is currently not publicly accessible, which hinders the future improvement of urban classification. The multiple-year high-resolution PFT maps developed by the European Space Agency's Climate Change Initiative could be used to further extend this dataset for a longer period (Harper et al., 2023).[¶]

736 soil properties, vegetation properties, and topographic factors contribute a lot to the spatial
737 heterogeneities of ELM water and energy simulations. Upscaling 1 km to a coarser 12 km
738 resolution, we observe significant spatial information loss, with SM experiencing an average loss
739 of 31%, and LH, ELR, and ASR experiencing around 50% information loss on average, (Figure
740 12). This conclusion is in line with the results of Vergopolan et al. (2022), which showed a
741 substantial loss of spatial information in soil moisture when upscaling from 30 m to 1 km resolution,
742 with an average loss of approximately 48% and up to 80% over the CONUS region. The XML
743 analysis reveals that the spatial variability and information loss of ELM2 simulations are
744 influenced by the spatial variability and information loss of the different variables of land surface
745 parameters, as well as the mean precipitation and temperature, (Figures 11 and 12). Our findings
746 highlight the critical role of land surface parameters in contributing to the spatial variability of
747 water and energy in land surface simulations, showcasing the value of the developed high-
748 resolution datasets. Another implementation example where our 1 km land surface parameters can
749 be beneficial is in hillslope-scale simulations, which are fundamental for organizing water, energy,
750 and biogeochemical processes (Fan et al., 2019). Krakauer et al. (2014) have highlighted the
751 significance of between-cell groundwater flow, which becomes comparable in magnitude to
752 recharge at grid spacings smaller than 10 km. Advancements have been made in ESMs to address
753 hillslope-scale processes, including the representation of intra-hillslope lateral subsurface flow
754 within grid cells in CLM5 (Swenson et al., 2019), the development of explicit lateral flow
755 processes between grid cells (Qiu et al., 2023), and the incorporation of topographic radiation
756 effects within and between grid cells (Hao et al., 2021). Another notable example is the integrated
757 hydrology-land surface model ParFlow-CLM, which incorporates three-dimensional groundwater
758 flow, two-dimensional overland flow, and land surface exchange processes (Maxwell, 2013).

Deleted: .

Deleted: .

761 ParFlow-CLM has demonstrated remarkable reliability in reproducing hydrologic processes, such
762 as its simulations at 3 km resolution for pan-European and 1 km resolution for CONUS (Naz et al.,
763 2023; O'Neill et al., 2021). More recently, Fang et al. (2022) coupled ParFlow with ELM and the
764 Functionally Assembled Terrestrial Ecosystem Simulator (FATES) to simulate carbon-hydrology
765 interactions at hillslope scale. By incorporating our 1 km datasets and leveraging these
766 advancements, we can improve simulations of hillslope-scale processes and enhance our
767 understanding of water and energy dynamics within ESMs.

768
769 ~~Additionally, the~~ new land surface parameters are also a timely resource for supporting the
770 emerging need for k-scale Earth system modeling, ~~particularly in improving land-atmosphere~~
771 ~~interaction processes~~. Representing the impact of spatial heterogeneity on land-atmosphere
772 interaction processes is a major challenge in Earth system modeling. Taking E3SM as an example,
773 researchers have proposed three key approaches to enhance spatial heterogeneity representation to
774 address this challenge. In line with these approaches, our newly developed 1 km land surface
775 parameters offer promising opportunities for improving land-atmosphere coupling within ESMs.
776 The first approach to enhance the representation of spatial heterogeneity is to directly conduct
777 simulations at high resolution. For instance, the Simple Cloud-Resolving E3SM Atmosphere
778 Model (SCREAM) has been used to perform global simulations at 3.25 km (Caldwell et al., 2021),
779 although the land surface parameters were based on coarser resolution datasets. By utilizing the
780 new 1 km land surface parameters, we can enhance the representation of land surface heterogeneity
781 within the ELM component of SCREAM, potentially improving modeling of land-atmosphere
782 coupling. The second and third approaches focus on improving the representation of land surface
783 heterogeneity within ESMs run at a coarse resolution while accounting for subgrid heterogeneity

Deleted: The

Deleted: .

786 in two different ways. In the second approach, the Cloud Layers Unified By Binormals (CLUBB)
787 has been implemented in E3SM Atmosphere Model (EAM) version 1 (Rasch et al., 2019;
788 Bogenschutz et al., 2013), to better account for subgrid atmospheric heterogeneity of turbulent
789 mixing, shallow convection, and cloud macrophysics. Recently, Huang et al. (2022) developed a
790 novel land-atmosphere coupling scheme in EAM that enables the communication of subgrid land
791 surface heterogeneity information to the atmosphere model with CLUBB, significantly impacting
792 boundary layer dynamics. The new 1km datasets can provide more accurate land surface
793 representations of the variability of individual patches and the inter-patch variability that were
794 used in Huang et al. (2022). The third approach is the Multiple Atmosphere Multiple Land (MAML)
795 approach used in the multiscale modeling framework (MMF) in which a cloud resolving model
796 (CRM) is embedded within each grid cell of the atmosphere (Baker et al., 2019; Lin et al., 2023;
797 Lee et al., 2023). In the MAML approach, each CRM column within the atmosphere grid is coupled
798 directly with its own independent land surface. This enables a more explicit representation of the
799 impact of spatial heterogeneity on land-atmosphere interactions within each grid and has shown
800 notable impacts on water and energy simulations (Baker et al., 2019; Lin et al., 2023). Lee et al.
801 (2023) highlighted the limitation of the current MAML approach, which utilizes the same land
802 surface characteristics for each land surface model interacting with the CRM column within the
803 same grid, which could lead to a weak representation of land-atmosphere interactions. To address
804 this limitation, incorporating the new 1 km land surface parameters within the MAML approach
805 can provide more detailed information about land surface heterogeneity, enabling a more accurate
806 capture of land-atmosphere interactions.

807

808 Evaluation of k-scale simulations, while essential, faces significant challenges as merely updating
809 the land surface input data to the new 1k parameters for k-scale simulations doesn't guarantee
810 improved model performance, which depends on both input data as well as model parameters and
811 structures. First, LSMs and ESMS that have been adapted for simulations at coarser resolutions
812 commensurate with the resolutions of previous land surface data require recalibration for effective
813 high-resolution modeling. This necessity for recalibration is echoed by Ruiz-Vásquez et al., (2023),
814 who noted that updating the ECMWF system with new land surface data did not inherently
815 improve performance, but improvements were seen after recalibrating key soil and vegetation-
816 related parameters. Second, high-resolution modeling requires the incorporation of new physical
817 processes crucial at finer scales. For example, hillslope-scale processes like lateral flow and
818 topography-radiation interactions are key to water and energy fluxes at high resolution (Han et al.,
819 2023; Hao et al., 2021). With increased heterogeneity at higher resolutions, larger differences in
820 land surface properties such as vegetation water use strategies requires more attention to plant
821 hydraulics besides the traditional focus on soil hydraulics for a more accurate depiction of plant
822 water use, as highlighted by Li et al., (2021). Third, the lack of high-resolution benchmarks for
823 large-scale applications, like k-scale atmospheric forcing data, remains a challenge, despite the
824 availability of relative coarse resolution global datasets such as ERA5_Land (Muñoz-Sabater et
825 al., 2021) and MSWX (Beck et al., 2021). Additionally, using soil moisture as an example, multiple
826 high-resolution datasets exhibit significantly different performance when compared to in-situ
827 measurements (Beck et al., 2021). Lastly, when evaluating simulations against benchmarks, it is
828 crucial not only to assess absolute differences using metrics like bias and root mean square error
829 but also to examine other metrics, such as the relationships between physical variables (e.g.,

830 rainfall vs. runoff; soil moisture vs. evapotranspiration), information loss, and the tail quantiles of
831 the probability distribution functions for simulations (e.g., extreme events).

832
833 There are certain opportunities for future development of 1k parameters. The urban extension may
834 vary based on data sources, urban definitions, and the algorithms employed, such as those derived
835 from harmonized nighttime lights (Zhao et al., 2022), global artificial impervious area (GAIA, Li
836 et al., 2020b; Gong et al., 2020), urban expansion (Liu et al., 2020; Kuang et al., 2021),
837 necessitating careful consideration in specific modeling applications. Additionally, urban
838 classification in J2010, based on global building height data, is limited by the lack of a consistent
839 and publicly accessible global dataset, despite available regional data for Europe (Frantz et al.,
840 2021), the US (Li et al., 2020a), and China (Cao and Huang, 2021; Yang and Zhao, 2022), thus
841 posing challenges to future urban classification enhancements. Incorporating local climate zones
842 offers a promising approach for urban classification and modeling. Moreover, the multiple-year
843 high-resolution PFT maps like the ones developed by the European Space Agency's Climate
844 Change Initiative could be used to further extend this dataset for a longer period (Harper et al.,
845 2023). Soil color, crucial for soil albedo and surface energy balance, lacks extensive global datasets
846 for ESMs modeling, but the global soil color map derived by Rizzo et al. (2023) offers potential
847 for further kilometer-scale ESMs and LSMs modeling.

848
849 The strategic aggregation of high-resolution parameters to coarser resolutions are crucial to
850 maintain accuracy and effectiveness in modeling applications. For instance, in soil properties, the
851 basic parameters (e.g., percent sand) are often utilized to derive secondary parameters (e.g.,
852 saturated water content). This aggregation procedure, whether performs before or after deriving

853 secondary parameters—known as 'aggregating first' and 'aggregating after'—is influenced by the
854 non-linear relationships between basic and derived parameters, with the latter method generally
855 preferred (Shangguan et al., 2014; Dai et al., 2019). Our study's initial approach in upscaling soil-
856 and topography-related parameters follows the 'aggregate first' approach, aligning with the
857 structure of models like ELM2 and CLM5. Conversely, models such as Common Land Model
858 (CoLM, Dai et al., 2003) and community Noah with multi-parameterization options (Noah-MP,
859 He et al., 2023; Niu et al., 2011; Yang et al., 2011) integrate secondary derived soil related
860 parameters directly as inputs, effectively demonstrating the advantages of the 'aggregating after'
861 approach. By leveraging secondary derived parameters from comprehensive databases such as
862 SoilGrids (Hengl et al., 2017) and GSDE (Shangguan et al., 2014), these models provide a valuable
863 framework for future development of models like ELM2 and CLM5 by directly integrating
864 secondary derived parameters.

865

866 **5. Data availability**

867 The 1 km land surface parameters are publicly available at
868 <https://doi.org/10.25584/PNNLDH/1986308> (Li et al., 2023).

869

870 **6. Conclusions**

871 We developed 1 km global land surface parameters using the latest available datasets covering
872 multiple years from 2001 to 2020. These parameters comprise four categories: LULC of PFTs and
873 non-vegetative land cover, vegetation properties, soil properties, and topographic factors. The new
874 1k parameters, when compared to the K2012 and ELM2/CLM5 default datasets, display
875 significant differences, indicating their potential superiority stemming from the utilization of latest
876 and more advanced data sources. The 1 km resolution ELM simulations conducted over CONUS
877 demonstrate the valuable capabilities of the new datasets in enabling k-scale land surface modeling.
878 Through scaling analysis of the 1 km resolution simulations within $0.5^\circ \times 0.5^\circ$ boxes where spatial
879 heterogeneity of the simulations is induced only by spatial heterogeneity of the land surface
880 parameters, we revealed the significant impact of land surface parameters on the spatial variability
881 of water and energy simulations. The spatial information loss of these simulations over CONUS
882 is significant when upscaling from 1 km to a coarser 12 km resolution, with an average ranging
883 from 31% to 54% and up to more than 90%. The XML analysis reveals that the spatial variability
884 and spatial information loss of ELM2 simulations are primarily impacted by the spatial variability
885 and information loss of soil properties, vegetation properties and topography factors, as well as the
886 mean climate conditions of precipitation and temperature. Furthermore, the spatial variability of
887 water and energy in the 1 km simulations is not dominated by the spatial heterogeneity of any land
888 surface parameters, suggesting the usefulness of the multi-parameter high-resolution land surface

Deleted: Conclusion

890 parameter dataset. The availability of 1 km land surface parameters is a valuable resource that
891 addresses the emerging needs of k-scale LSMs and ESMs modeling. By providing accurate and
892 precise information, these 1 km land surface parameters will significantly enhance our
893 understanding of the water, carbon, and energy cycles under global change.

894

895 **Author contributions**

896 LL, GB, and DH designed the study, processed the datasets, conducted experiments, and drafted
897 the manuscript. LRL contributed to the conceptual design, discussion of results, and manuscript
898 revisions.

899

900 **Acknowledgments**

901 This study is supported by the US Department of Energy (DOE) Office of Science Biological and
902 Environmental Research as part of the Regional and Global Model Analysis (RGMA) program
903 area through the collaborative, multi-program Integrated Coastal Modeling (ICoM) project. This
904 study used DOE's Biological and Environmental Research Earth System Modeling program's
905 Compy computing cluster at Pacific Northwest National Laboratory. ~~Pacific Northwest National~~
906 Laboratory is operated for the US Department of Energy by Battelle Memorial Institute under
907 contract DE-AC05-76RL01830. DH acknowledges the support from the US DOE, Office of
908 Science, Office of Biological and Environmental Research, Earth System Model Development
909 program area, as part of the Climate Process Team projects. Our thanks to Ye Liu and Teklu Tesfa
910 at PNNL for guidance on the canopy height dataset and K2012 datasets, respectively. We deeply
911 appreciate the reviewers for their valuable insights and suggestions.

912

913 **Financial support**

914 This work was supported by the Regional and Global Modeling and Analysis program area of the US
915 Department of Energy, Office of Science, Office of Biological and Environmental Research, as
916 part of the multi-program, collaborative integrated Coastal Modeling (ICoM) project (grant no.
917 KP1703110/75415).

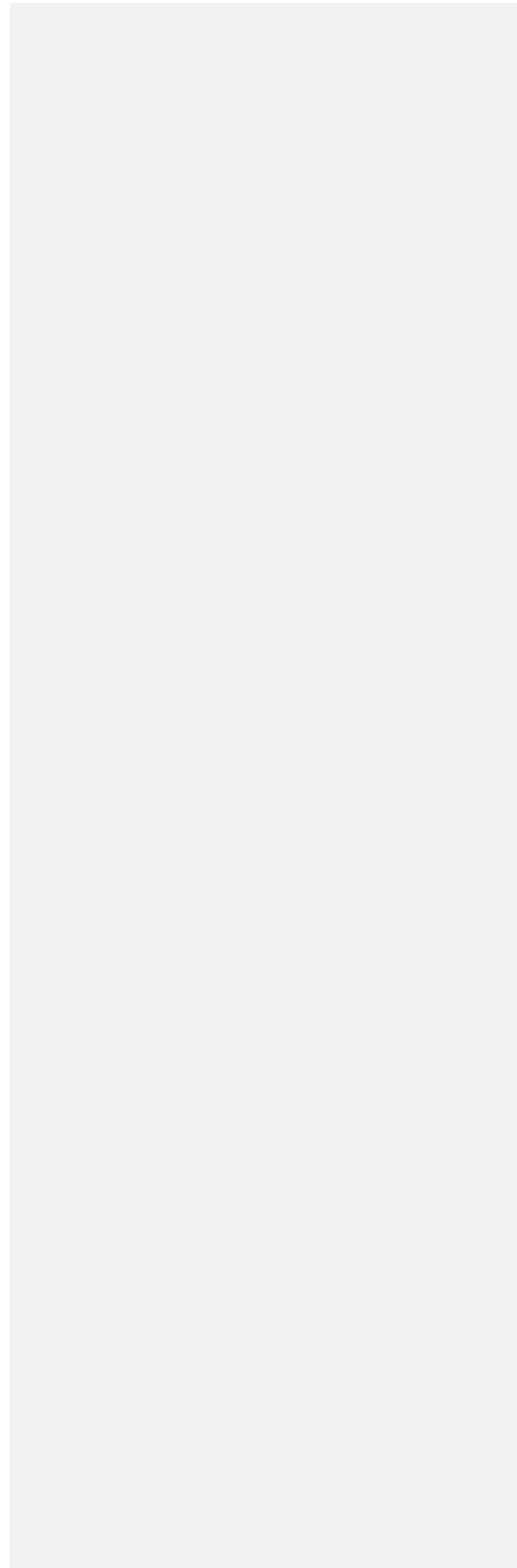
Deleted: We thank Ye Liu at PNNL for providing suggestions on processing the canopy height dataset.

920

921 **Competing interests**

922 At least one of the (co-)authors is a member of the editorial board of the Earth System Science

923 Data. The authors have no other competing interests to declare.



924 **Reference**

925 Arendt, A., Bliss, A., Bolch, T., et al.: Randolph Glacier Inventory—A Dataset of Global Glacier
926 Outlines Version: 1.0, Global Land Ice Measurements from Space, Boulder Colorado, USA.
927 Digital Media, 2012.

928 Baker, I. T., Denning, A. S., Dazlich, D. A., Harper, A. B., Branson, M. D., Randall, D. A.,
929 Phillips, M. C., Haynes, K. D., and Gallup, S. M.: Surface-Atmosphere Coupling Scale, the Fate
930 of Water, and Ecophysiological Function in a Brazilian Forest, *J Adv Model Earth Sy*, 11, 2523–
931 2546, <https://doi.org/10.1029/2019ms001650>, 2019.

932 Batjes, N.H.: ISRIC-WISE derived soil properties on a 5 by 5 arc-minutes global grid. Report
933 2006/02, available through : <http://www.isric.org>, 2006.

934 [Beck, H. E., Van Dijk, A. I., Larraondo, P. R., McVicar, T. R., Pan, M., Dutra, E., & Miralles, D.
935 G.: MSWX: Global 3-hourly 0.1 bias-corrected meteorological data including near-real-time
936 updates and forecast ensembles, *BAMS*, 103\(3\), E710-E732, \[https://doi.org/10.1175/BAMS-D-
21-0145.1\]\(https://doi.org/10.1175/BAMS-D-
937 21-0145.1\), 2022.](#)

938 [Beck, H. E., Pan, M., Miralles, D. G., Reichle, R. H., Dorigo, W. A., Hahn, S., Sheffield, J.,
939 Karthikeyan, L., Balsamo, G., Parinussa, R. M., van Dijk, A. I. J. M., Du, J., Kimball, J. S.,
940 Vergopolan, N., and Wood, E. F.: Evaluation of 18 satellite- and model-based soil moisture
941 products using in situ measurements from 826 sensors, *Hydrol Earth Syst Sci*, 25, 17–40,
942 <https://doi.org/10.5194/hess-25-17-2021>, 2021.](#)

943 Bogenschutz, P. A., Gettelman, A., Morrison, H., Larson, V. E., Craig, C., and Schanen, D. P.:
944 Higher-Order Turbulence Closure and Its Impact on Climate Simulations in the Community
945 Atmosphere Model, *J Climate*, 26, 9655–9676, <https://doi.org/10.1175/jcli-d-13-00075.1>, 2013.

946 Bonan, G. B., Oleson, K. W., Vertenstein, M., Levis, S., Zeng, X., Dai, Y., Dickinson, R. E., and
947 Yang, Z.-L.: The Land Surface Climatology of the Community Land Model Coupled to the
948 NCAR Community Climate Model*, *J Climate*, 15, 3123–3149, [https://doi.org/10.1175/1520-
0442\(2002\)015<3123:tlscot>2.0.co;2](https://doi.org/10.1175/1520-
949 0442(2002)015<3123:tlscot>2.0.co;2), 2002.

950 Bonan, G. B., Levis, S., Kergoat, L., & Oleson, K. W.: Landscapes as patches of plant functional
951 types: An integrating concept for climate and ecosystem models. *Global Biogeochemical Cycles*,
952 16(2), 5-1–5-23. <https://doi.org/10.1029/2000gb001360>, 2002

953 Bou-Zeid, E., Anderson, W., Katul, G. G., and Mahrt, L.: The Persistent Challenge of Surface
954 Heterogeneity in Boundary-Layer Meteorology: A Review, *Bound-lay Meteorol*, 177, 227–245,
955 <https://doi.org/10.1007/s10546-020-00551-8>, 2020.

956 Caldwell, P. M., Mametjanov, A., Tang, Q., Roedel, L. P. V., Golaz, J., Lin, W., Bader, D. C.,
957 Keen, N. D., Feng, Y., Jacob, R., Maltrud, M. E., Roberts, A. F., et al.: The DOE E3SM Coupled
958 Model Version 1: Description and Results at High Resolution, *J Adv Model Earth Sy*, 11, 4095–
959 4146, <https://doi.org/10.1029/2019ms001870>, 2019.

Moved (insertion) [2]

Moved (insertion) [3]

960 Caldwell, P. M., Terai, C. R., Hillman, B., Keen, N. D., Bogenschutz, P., Lin, W., et al.:
 961 Convection-Permitting Simulations With the E3SM Global Atmosphere Model, *J Adv Model*
 962 *Earth Sy*, 13, <https://doi.org/10.1029/2021ms002544>, 2021.

963 Cao, Y. and Huang, X.: A deep learning method for building height estimation using high-
 964 resolution multi-view imagery over urban areas: A case study of 42 Chinese cities, *Remote Sens*
 965 *Environ*, 264, 112590, <https://doi.org/10.1016/j.rse.2021.112590>, 2021.

966 Chaney, N. W., Huijgevoort, M. H. J. V., Shevliakova, E., Malyshev, S., Milly, P. C. D.,
 967 Gauthier, P. P. G., and Sulman, B. N.: Harnessing big data to rethink land heterogeneity in Earth
 968 system models, *Hydrol Earth Syst Sc*, 22, 3311–3330, [https://doi.org/10.5194/hess-22-3311-](https://doi.org/10.5194/hess-22-3311-2018)
 969 [2018](https://doi.org/10.5194/hess-22-3311-2018), 2018.

970 Change, N. C.: Think big and model small, *Nat Clim Change*, 12, 493–493,
 971 <https://doi.org/10.1038/s41558-022-01399-1>, 2022.

972 ~~Chen, T. and Guestrin, C.: XGBoost: A Scalable Tree Boosting System, *Proc 22nd Acm Sigkdd*
 973 *Int Conf Knowl Discov Data Min*, 785–794, <https://doi.org/10.1145/2939672.2939785>, 2016.~~

974 ~~Dai, Y., Zeng, X., Dickinson, R. E., Baker, I., Bonan, G. B., Bosilovich, M. G., et al.: The
 975 common land model, *BAMS*, 84(8), 1013-1024, <https://doi.org/10.1175/BAMS-84-8-1013>,
 976 2003.~~

977 ~~Dai, Y., Shangguan, W., Wei, N., Xin, Q., Yuan, H., Zhang, S., Liu, S., Lu, X., Wang, D., and
 978 Yan, F.: A Review of the Global Soil Property Maps for Earth System Models, *SOIL*, 5, 137-
 979 158, <https://doi.org/10.5194/soil-5-137-2019>, 2019.~~

980 ~~Defries, R. S., Hansen, M. C., Townshend, J. R. G., Janetos, A. C., and Loveland, T. R.: A new
 981 global 1-km dataset of percentage tree cover derived from remote sensing: GLOBAL
 982 PERCENTAGE TREE COVER FROM REMOTE SENSING, *Global Change Biol*, 6, 247–254,
 983 <https://doi.org/10.1046/j.1365-2486.2000.00296.x>, 2000.~~

984 Dozier, J.: Revisiting Topographic Horizons in the Era of Big Data and Parallel Computing, *Ieee*
 985 *Geosci Remote S*, 19, 1–5, <https://doi.org/10.1109/lgrs.2021.3125278>, 2022.

986 Fan, Y., Clark, M., Lawrence, D. M., Swenson, S., Band, L. E., Brantley, S. L., et al.: Hillslope
 987 Hydrology in Global Change Research and Earth System Modeling, *Water Resour Res*, 55,
 988 1737–1772, <https://doi.org/10.1029/2018wr023903>, 2019.

989 Frantz, D., Schug, F., Okujeni, A., Navacchi, C., Wagner, W., Linden, S. van der, and Hostert,
 990 P.: National-scale mapping of building height using Sentinel-1 and Sentinel-2 time series,
 991 *Remote Sens Environ*, 252, 112128, <https://doi.org/10.1016/j.rse.2020.112128>, 2021.

992 Friedl, M. A., McIver, D. K., Hodges, J. C. F., Zhang, X. Y., Muchoney, D., Strahler, A. H.,
 993 Woodcock, C. E., Gopal, S., Schneider, A., Cooper, A., Baccini, A., Gao, F., and Schaaf, C.:

Moved (insertion) [4]

Moved up [3]: J.

Deleted: J., Hagos, S., Xiao, H., Fast,

Deleted: D., and Feng, Z.: Characterization of Surface Heterogeneity-Induced Convection Using Cluster Analysis, *J Geophys Res Atmospheres*, 125, <https://doi.org/10.1029/2020jd032550>, 2020

Field Code Changed

Deleted: Chen,

Moved up [4]: T. and Guestrin, C.: XGBoost: A Scalable Tree Boosting System, *Proc 22nd Acm Sigkdd Int Conf Knowl Discov Data Min*, 785–794, <https://doi.org/10.1145/2939672.2939785>, 2016

Deleted: .

1007 Global land cover mapping from MODIS: algorithms and early results, *Remote Sens Environ*,
1008 83, 287–302, [https://doi.org/10.1016/s0034-4257\(02\)00078-0](https://doi.org/10.1016/s0034-4257(02)00078-0), 2002.

1009 Friedl, M. A., Sulla-Menashe, D., Tan, B., Schneider, A., Ramankutty, N., Sibley, A., and
1010 Huang, X.: MODIS Collection 5 global land cover: Algorithm refinements and characterization
1011 of new datasets, *Remote Sens Environ*, 114, 168–182, <https://doi.org/10.1016/j.rse.2009.08.016>,
1012 2010.

1013 Friedl, M., Sulla-Menashe, D.: MCD12Q1 MODIS/Terra+Aqua Land Cover Type Yearly L3
1014 Global 500m SIN Grid V006 [Data set]. NASA EOSDIS Land Processes DAAC. Accessed
1015 2022-11-21 from <https://doi.org/10.5067/MODIS/MCD12Q1.006>, 2019.

1016 Giorgi, F. and Avissar, R.: Representation of heterogeneity effects in Earth system modeling:
1017 Experience from land surface modeling, *Rev Geophys*, 35, 413–437,
1018 <https://doi.org/10.1029/97rg01754>, 1997.

1019 Gorelick, N., Hancher, M., Dixon, M., Ilyushchenko, S., Thau, D., & Moore, R.: Google Earth
1020 Engine: Planetary-scale geospatial analysis for everyone. *Remote Sensing of Environment*, 202,
1021 18–27. <https://doi.org/10.1016/j.rse.2017.06.031>, 2017.

1022 Gong, P., Li, X., Wang, J., Bai, Y., Chen, B., Hu, T., Liu, X., Xu, B., Yang, J., Zhang, W., and
1023 Zhou, Y.: Annual maps of global artificial impervious area (GAIA) between 1985 and 2018,
1024 *Remote Sens Environ*, 236, 111510, <https://doi.org/10.1016/j.rse.2019.111510>, 2020.

1025 Gorelick, N., Hancher, M., Dixon, M., Ilyushchenko, S., Thau, D., and Moore, R.: Google Earth
1026 Engine: Planetary-scale geospatial analysis for everyone, *Remote Sens Environ*, 202, 18–27,
1027 <https://doi.org/10.1016/j.rse.2017.06.031>, 2017.

1028 Hansen, M. C., DeFries, R. S., Townshend, J. R. G., Carroll, M., Dimiceli, C., and Sohlberg, R.
1029 A.: Global Percent Tree Cover at a Spatial Resolution of 500 Meters: First Results of the MODIS
1030 Vegetation Continuous Fields Algorithm, *Earth Interact*, 7, 1–15, [https://doi.org/10.1175/1087-3562\(2003\)007<0001:gptcaa>2.0.co;2](https://doi.org/10.1175/1087-3562(2003)007<0001:gptcaa>2.0.co;2), 2003.

1032 Hao, D., Bisht, G., Huang, M., Ma, P., Tesfa, T., Lee, W., Gu, Y., and Leung, L. R.: Impacts of
1033 Sub-Grid Topographic Representations on Surface Energy Balance and Boundary Conditions in
1034 the E3SM Land Model: A Case Study in Sierra Nevada, *J Adv Model Earth Sy*, 14,
1035 <https://doi.org/10.1029/2021ms002862>, 2022.

1036 Harper, K. L., Lamarche, C., Hartley, A., Peylin, P., Ottlé, C., Bastrikov, V., Martín, R. S.,
1037 Bohnenstengel, S. I., Kirches, G., Boettcher, M., Shevchuk, R., Brockmann, C., and Defourny,
1038 P.: A 29-year time series of annual 300 m resolution plant-functional-type maps for climate
1039 models, *Earth Syst Sci Data*, 15, 1465–1499, <https://doi.org/10.5194/essd-15-1465-2023>, 2023.

1040 Hengl, T., Jesus, J. M. de, Heuvelink, G. B. M., Gonzalez, M. R., Kilibarda, M., Blagotić, A.,
1041 Shangquan, W., Wright, M. N., et al.: SoilGrids250m: Global gridded soil information based on
1042 machine learning, *Plos One*, 12, e0169748, <https://doi.org/10.1371/journal.pone.0169748>, 2017.

1043 Hewitt, H., Fox-Kemper, B., Pearson, B., Roberts, M., and Klocke, D.: The small scales of the
1044 ocean may hold the key to surprises, *Nat Clim Change*, 12, 496–499,
1045 <https://doi.org/10.1038/s41558-022-01386-6>, 2022.

1046 [He, C., Valayamkunnath, P., Barlage, M., Chen, F., Gochis, D., Cabell, R., Schneider, T.,](#)
1047 [Rasmussen, R., Niu, G.-Y., Yang, Z.-L., Niyogi, D., and Ek, M.: Modernizing the open-source](#)
1048 [community Noah with multi-parameterization options \(Noah-MP\) land surface model \(version](#)
1049 [5.0\) with enhanced modularity, interoperability, and applicability, *Geosci Model Dev*, 16, 5131–](#)
1050 [5151, <https://doi.org/10.5194/gmd-16-5131-2023>, 2023.](#)

1051 Hijmans, R. J., Cameron, S. E., Parra, J. L., Jones, P. G., and Jarvis, A.: Very high resolution
1052 interpolated climate surfaces for global land areas, *International Journal of Climatology*, 25,
1053 1965–1978, <https://doi.org/10.1002/joc.1276>, 2005.

1054 Hu, Z., Islam, S., and Cheng, Y.: Statistical characterization of remotely sensed soil moisture
1055 images, *Remote Sens Environ*, 61, 310–318, [https://doi.org/10.1016/s0034-4257\(97\)89498-9](https://doi.org/10.1016/s0034-4257(97)89498-9),
1056 1997.

1057 Huang, M., Ma, P.-L., Chaney, N. W., Hao, D., Bisht, G., Fowler, M. D., Larson, V. E., and
1058 Leung, L. R.: Representing surface heterogeneity in land-atmosphere coupling in E3SMv1
1059 single-column model over ARM SGP during summertime, *Geoscientific Model Dev Discuss*,
1060 2022, 1–20, <https://doi.org/10.5194/gmd-2021-421>, 2022.

1061 [Huang, F., Jiang, S., Zhan, W., Bechtel, B., Liu, Z., Demuzere, M.: Mapping local climate zones](#)
1062 [for cities: A large review, *Remote Sens. Environ.*, 292, 113573,](#)
1063 <https://doi.org/10.1016/j.rse.2023.113573>, 2023.

1064 Hugelius, G., Tarnocai, C., Broll, G., Canadell, J. G., Kuhry, P., and Swanson, D. K.: The
1065 Northern Circumpolar Soil Carbon Database: spatially distributed datasets of soil coverage and
1066 soil carbon storage in the northern permafrost regions, *Earth Syst. Sci. Data*, 5, 3–13,
1067 <https://doi.org/10.5194/essd-5-3-2013>, 2013.

1068 IGBP: Global Soil Data Task (IGBP-DIS, ISO-image of CD). International Geosphere-Biosphere
1069 Program, PANGAEA, <https://doi.org/10.1594/PANGAEA.869912>, 2000.

1070 Jackson, T. L., Feddema, J. J., Oleson, K. W., Bonan, G. B., and Bauer, J. T.: Parameterization
1071 of Urban Characteristics for Global Climate Modeling, *Ann Assoc Am Geogr*, 100, 848–865,
1072 <https://doi.org/10.1080/00045608.2010.497328>, 2010.

1073 Jarvis, A., H.I. Reuter, A. Nelson, E. Guevara.: Hole-filled SRTM for the globe Version 4,
1074 available from the CGIAR-CSI SRTM 90m Database: <https://srtm.csi.cgiar.org>, 2008.

1075 Ji, P. and Yuan, X.: High-Resolution Land Surface Modeling of Hydrological Changes Over the
1076 Sanjiangyuan Region in the Eastern Tibetan Plateau: 2. Impact of Climate and Land Cover
1077 Change, *J Adv Model Earth Sy*, 10, 2829–2843, <https://doi.org/10.1029/2018ms001413>, 2018.

1078 Ji, P., Yuan, X., Shi, C., Jiang, L., Wang, G., and Yang, K.: A Long-Term Simulation of Land
1079 Surface Conditions at High Resolution over Continental China, *J Hydrometeorol*, 24, 285–314,
1080 <https://doi.org/10.1175/jhm-d-22-0135.1>, 2023.

1081 Ke, Y., Leung, L. R., Huang, M., Coleman, A. M., Li, H., and Wigmosta, M. S.: Development of
1082 high resolution land surface parameters for the Community Land Model, *Geosci Model Dev*, 5,
1083 1341–1362, <https://doi.org/10.5194/gmd-5-1341-2012>, 2012.

1084 Ke, Y., Leung, L. R., Huang, M., and Li, H.: Enhancing the representation of subgrid land
1085 surface characteristics in land surface models, *Geosci Model Dev*, 6, 1609–1622,
1086 <https://doi.org/10.5194/gmd-6-1609-2013>, 2013.

1087 Kim, H.: Global Soil Wetness Project Phase 3 Atmospheric Boundary Conditions (Experiment 1)
1088 [Data set]. Data Integration and Analysis System (DIAS). <https://doi.org/10.20783/DIAS.501>,
1089 2017.

1090 Kourzeneva, E.: Global dataset for the parameterization of lakes in Numerical Weather
1091 Prediction and Climate modeling. ALADIN Newsletter, No 37, July-December, 2009, F.
1092 Bouttier and C. Fischer, Eds., Meteo-France, Toulouse, France, 46-53, 2009.

1093 Kourzeneva, E.: External data for lake parameterization in Numerical Weather Prediction and
1094 climate modeling. *Boreal Environment Research*, 15, 165-177, 2010.

1095 Krakauer, N. Y., Li, H., and Fan, Y.: Groundwater flow across spatial scales: importance for
1096 climate modeling, *Environ Res Lett*, 9, 034003, <https://doi.org/10.1088/1748-9326/9/3/034003>,
1097 2014.

1098 Kuang, W., Du, G., Lu, D., Dou, Y., Li, X., Zhang, S., Chi, W., Dong, J., Chen, G., Yin, Z., Pan,
1099 T., Hamdi, R., Hou, Y., Chen, C., Li, H., and Miao, C.: Global observation of urban expansion
1100 and land-cover dynamics using satellite big-data, *Sci Bull*, 66, 297–300,
1101 <https://doi.org/10.1016/j.scib.2020.10.022>, 2021.

1102 Lang, N., Jetz, W., Schindler, K., and Wegner, J. D.: A high-resolution canopy height model of
1103 the Earth, *Nat Ecol Evol*, <https://doi.org/10.1038/s41559-023-02206-6>, 2023.

1104 Lawrence, D. M., Fisher, R. A., Koven, C. D., Oleson, K. W., Swenson, S. C., Bonan, G., et al.:
1105 The Community Land Model Version 5: Description of New Features, Benchmarking, and
1106 Impact of Forcing Uncertainty, *J Adv Model Earth Sy*, 11, 4245–4287,
1107 <https://doi.org/10.1029/2018ms001583>, 2019.

1108 Lawrence, D., Fisher, R., Koven, C., Oleson, K., Swenson, S., et al. (2018). Technical
1109 description of version 5.0 of the Community Land Model (CLM). National Center for
1110 Atmospheric Research, University Corporation for Atmospheric Research, Boulder, CO.
1111 https://escomp.github.io/ctsm-docs/versions/release-clm5.0/html/tech_note/index.html

Deleted: , Arxiv

Deleted: <https://doi.org/10.48550/arxiv.2204.08322>, 2022

1114 Lee, J., Hannah, W. M., and Bader, D. C.: Representation of atmosphere induced heterogeneity
1115 in land – atmosphere interactions in E3SM-MMFv2, *Geoscientific Model Dev Discuss*, 2023, 1–
1116 21, <https://doi.org/10.5194/gmd-2023-55>, 2023.

1117 Leng, G., Huang, M., Tang, Q., Sacks, W. J., Lei, H., and Leung, L. R.: Modeling the effects of
1118 irrigation on land surface fluxes and states over the conterminous United States: Sensitivity to
1119 input data and model parameters, *J Geophys Res Atmospheres*, 118, 9789–9803,
1120 <https://doi.org/10.1002/jgrd.50792>, 2013.

1121 Leung, L. R., Bader, D. C., Taylor, M. A., and McCoy, R. B.: An Introduction to the E3SM
1122 Special Collection: Goals, Science Drivers, Development, and Analysis, *J Adv Model Earth Sy*,
1123 12, <https://doi.org/10.1029/2019ms001821>, 2020.

1124 Li, L., [Yang, Z.](#), [Matheny, A. M.](#), [Zheng, H.](#), [Swenson, S. C.](#), [Lawrence, D. M.](#), [Barlage, M.](#),
1125 [Yan, B.](#), [McDowell, N. G.](#), and [Leung, L. R.](#): Representation of Plant Hydraulics in the Noah-
1126 [MP Land Surface Model: Model Development and Multiscale Evaluation](#), *J Adv Model Earth*
1127 [Sy](#), 13, <https://doi.org/10.1029/2020ms002214>, 2021.

1128 [Li, L.](#), Bisht, G., and Leung, L. R.: Spatial heterogeneity effects on land surface modeling of
1129 water and energy partitioning, *Geosci Model Dev*, 15, 5489–5510, <https://doi.org/10.5194/gmd-15-5489-2022>, 2022.

1131 Li, X., Zhou, Y., Gong, P., Seto, K. C., and Clinton, N.: Developing a method to estimate
1132 building height from Sentinel-1 data, *Remote Sens Environ*, 240, 111705,
1133 <https://doi.org/10.1016/j.rse.2020.111705>, 2020a.

1134 Li, X., Gong, P., Zhou, Y., Wang, J., Bai, Y., Chen, B., Hu, T., Xiao, Y., et al.: Mapping global
1135 urban boundaries from the global artificial impervious area (GAIA) data, *Environ Res Lett*, 15,
1136 094044, <https://doi.org/10.1088/1748-9326/ab9be3>, 2020b.

1137 Li, L., Bisht, G., Hao, D., Leung, L.R.: Global 1km Land Surface Parameters for Kilometer
1138 Scale Earth System Modeling, Pacific Northwest National Laboratory DataHub [data set],
1139 <https://doi.org/10.25584/PNNLDH/1986308>, 2023.

1140 Lin, G., Leung, L. R., Lee, J., Harrop, B. E., Baker, I. T., Branson, M. D., Denning, A. S., Jones,
1141 C. R., Ovchinnikov, M., Randall, D. A., and Yang, Z.: Modeling Land-Atmosphere Coupling at
1142 Cloud-Resolving Scale Within the Multiple Atmosphere Multiple Land (MAML) Framework in
1143 SP-E3SM, *J Adv Model Earth Sy*, 15, <https://doi.org/10.1029/2022ms003101>, 2023.

1144 Liu, S., Shao, Y., Kunoth, A., and Simmer, C.: Impact of surface-heterogeneity on atmosphere
1145 and land-surface interactions, *Environ Modell Softw*, 88, 35–47,
1146 <https://doi.org/10.1016/j.envsoft.2016.11.006>, 2017.

1147 Liu, X., Huang, Y., Xu, X., Li, X., Li, X., Ciais, P., Lin, P., et al.: High-spatiotemporal-
1148 resolution mapping of global urban change from 1985 to 2015, *Nat Sustain*, 3, 564–570,
1149 <https://doi.org/10.1038/s41893-020-0521-x>, 2020.

1150 Lundberg, S. and Lee, S.-I.: A Unified Approach to Interpreting Model Predictions, Arxiv, 2017.

1151 Lundberg, S. M., Nair, B., Vavilala, M. S., Horibe, M., Eisses, M. J., Adams, T., Liston, D. E.,
1152 Low, D. K.-W., Newman, S.-F., Kim, J., and Lee, S.-I.: Explainable machine-learning
1153 predictions for the prevention of hypoxaemia during surgery, *Nat Biomed Eng*, 2, 749–760,
1154 <https://doi.org/10.1038/s41551-018-0304-0>, 2018.

1155 Lundberg, S. M., Erion, G., Chen, H., DeGrave, A., Prutkin, J. M., Nair, B., Katz, R.,
1156 Himmelfarb, J., Bansal, N., and Lee, S.-I.: From local explanations to global understanding with
1157 explainable AI for trees, *Nat Mach Intell*, 2, 56–67, <https://doi.org/10.1038/s42256-019-0138-9>,
1158 2020.

1159 Mälicke, M., Hassler, S. K., Blume, T., Weiler, M., and Zehe, E.: Soil moisture: variable in
1160 space but redundant in time, *Hydrol Earth Syst Sc*, 24, 2633–2653, [https://doi.org/10.5194/hess-](https://doi.org/10.5194/hess-24-2633-2020)
1161 [24-2633-2020](https://doi.org/10.5194/hess-24-2633-2020), 2020.

1162 Maxwell, R. M.: A terrain-following grid transform and preconditioner for parallel, large-scale,
1163 integrated hydrologic modeling, *Adv Water Resour*, 53, 109–117,
1164 <https://doi.org/10.1016/j.advwatres.2012.10.001>, 2013.

1165 [Morisette, J. T., Baret, F., Privette, J. L., Myneni, R. B., Nickeson, J. E., et al.: Validation of](https://doi.org/10.1109/TGRS.2006.872529)
1166 [global moderate-resolution LAI products: A framework proposed within the CEOS land product](https://doi.org/10.1109/TGRS.2006.872529)
1167 [validation subgroup, *IEEE Trans Geosci Remote Sens*, 44\(7\), 1804-1817.](https://doi.org/10.1109/TGRS.2006.872529)
1168 <https://doi.org/10.1109/TGRS.2006.872529>, 2006.

1169 [Muñoz-Sabater, J., Dutra, E., Agustí-Panareda, A., Albergel, C., Arduini, G., Balsamo, G.,](https://doi.org/10.5194/essd-13-4349-2021)
1170 [Boussetta, S., Choulga, M., Harrigan, S., Hersbach, H., Martens, B., Miralles, D. G., Piles, M.,](https://doi.org/10.5194/essd-13-4349-2021)
1171 [Rodríguez-Fernández, N. J., Zsoter, E., Buontempo, C., and Thépaut, J.-N.: ERA5-Land: a state-](https://doi.org/10.5194/essd-13-4349-2021)
1172 [of-the-art global reanalysis dataset for land applications, *Earth Syst Sci Data*, 13, 4349–4383,](https://doi.org/10.5194/essd-13-4349-2021)
1173 <https://doi.org/10.5194/essd-13-4349-2021>, 2021.

1174 Myneni, R. B., Hoffman, S., Knyazikhin, Y., Privette, J. L., Glassy, J., Tian, Y., Wang, Y., Song,
1175 X., Zhang, Y., Smith, G. R., Lotsch, A., Friedl, M., Morisette, J. T., Votava, P., Nemani, R. R.,
1176 and Running, S. W.: Global products of vegetation leaf area and fraction absorbed PAR from
1177 year one of MODIS data, *Remote Sens Environ*, 83, 214–231, [https://doi.org/10.1016/s0034-](https://doi.org/10.1016/s0034-4257(02)00074-3)
1178 [4257\(02\)00074-3](https://doi.org/10.1016/s0034-4257(02)00074-3), 2002.

1179 Myneni, R., Knyazikhin, Y., Park, T. (2021). MODIS/Terra+Aqua Leaf Area Index/FPAR 4-Day
1180 L4 Global 500m SIN Grid V061 [Data set]. NASA EOSDIS Land Processes DAAC. Accessed
1181 2022-11-21 from <https://doi.org/10.5067/MODIS/MCD15A3H.061>

1182 Naz, B. S., Sharples, W., Ma, Y., Goergen, K., and Kollet, S.: Continental-scale evaluation of a
1183 fully distributed coupled land surface and groundwater model, ParFlow-CLM (v3.6.0), over
1184 Europe, *Geosci Model Dev*, 16, 1617–1639, <https://doi.org/10.5194/gmd-16-1617-2023>, 2023.

1185 [Niu, G. Y., Yang, Z. L., Mitchell, K. E., Chen, F., Ek, M. B., Barlage, M., et al.: The community](#)
1186 [Noah land surface model with multiparameterization options \(Noah-MP\): 1. Model description](#)
1187 [and evaluation with local-scale measurements, J Geophys Res Atmos, 116\(D12\),](#)
1188 <https://doi.org/10.1029/2010JD015139>, 2011

Deleted: Nitta, T., Arakawa, T., Hatono, M., Takeshima,

1189 [O'Neill, M. M. F., Tijerina, D. T., Condon, L. E., and Maxwell, R. M.: Assessment of the](#)
1190 [ParFlow-CLM CONUS 1.0 integrated hydrologic model: evaluation of hyper-resolution water](#)
1191 [balance components across the contiguous United States, Geosci Model Dev, 14, 7223–7254,](#)
1192 <https://doi.org/10.5194/gmd-14-7223-2021>, 2021.

Moved up [2]: A.,

Deleted: & Yoshimura, K: Development of integrated land simulator, Prog Earth Planet Sci, 7(1), 1-14, <https://doi.org/10.1186/s40645-020-00383-7>, 2020.

1193 [Poggio, L., Sousa, L. M. de, Batjes, N. H., Heuvelink, G. B. M., Kempen, B., Ribeiro, E., and](#)
1194 [Rossiter, D.: SoilGrids 2.0: producing soil information for the globe with quantified spatial](#)
1195 [uncertainty, Soil, 7, 217–240, https://doi.org/10.5194/soil-7-217-2021](#), 2021.

1196 [Qiu, H., Bisht, G., Li, L., Hao, D., and Xu, D.: Development of Inter-Grid Cell Lateral](#)
1197 [Unsaturated and Saturated Flow Model in the E3SM Land Model \(v2.0\), Egusphere, 2023, 1–31,](#)
1198 <https://doi.org/10.5194/egusphere-2023-375>, 2023.

1199 [Rabus, B., Eineder, M., Roth, A., & Bamler, R.: The shuttle radar topography mission—A new](#)
1200 [class of digital elevation models acquired by spaceborne radar. ISPRS Journal of](#)
1201 [Photogrammetry and Remote Sensing, 57\(4\), 241–262. https://doi.org/10.1016/s0924-](#)
1202 [2716\(02\)00124-7](https://doi.org/10.1016/s0924-2716(02)00124-7), 2003.

1203 [Ramankutty, N. and Foley, J. A.: Estimating historical changes in global land cover: Croplands](#)
1204 [from 1700 to 1992, Global Biogeochem Cy, 13, 997–1027,](#)
1205 <https://doi.org/10.1029/1999gb900046>, 1999.

1206 [Rasch, P. J., Xie, S., Ma, P. -L., Lin, W., Wang, H., Tang, Q., Burrows, S. M., Caldwell, P., et](#)
1207 [al.: An Overview of the Atmospheric Component of the Energy Exascale Earth System Model, J](#)
1208 [Adv Model Earth Sy, 11, 2377–2411, https://doi.org/10.1029/2019ms001629](#), 2019.

1209 [Rastner, P., Bolch, T., Mölg, N., Machguth, H., Le Bris, R., and Paul, F.: The first complete](#)
1210 [inventory of the local glaciers and ice caps on Greenland, The Cryosphere, 6, 1483–1495,](#)
1211 <https://doi.org/10.5194/tc-6-1483-2012>, 2012.

1212 [Rizzo, R., Wadoux, A. M. C., Demattê, J. A., Minasny, B., Barrón, V., Ben-Dor, E., ... &](#)
1213 [Salama, E. S. M.: Remote sensing of the Earth's soil color in space and time, Remote Sens](#)
1214 [Environ, 299, 113845, https://doi.org/10.1016/j.rse.2023.113845](#), 2023.

1215 [Rouf, T., Maggioni, V., Mei, Y., and Houser, P.: Towards hyper-resolution land-surface](#)
1216 [modeling of surface and root zone soil moisture, J Hydrol, 594, 125945,](#)
1217 <https://doi.org/10.1016/j.jhydrol.2020.125945>, 2021.

1218 [Ruiz-Vásquez, M., O. S., Arduini, G., Boussetta, S., Brenning, A., et al: Impact of updating](#)
1219 [vegetation information on land surface model performance, J. Geophys. Res. Atmos., 128\(21\),](#)
1220 [e2023JD039076, https://doi.org/10.1029/2023JD039076](https://doi.org/10.1029/2023JD039076), 2023.

- 1226 [Shangguan, W., Dai, Y., Duan, Q., Liu, B., and Yuan, H.: A Global Soil Dataset for Earth](#)
1227 [System Modeling, *J Adv Model Earth Syst*, 6, 249-263. <https://doi.org/10.1002/2013MS000293>,](#)
1228 [2014.](#)
- 1229 Simard, M., Pinto, N., Fisher, J. B., and Baccini, A.: Mapping forest canopy height globally with
1230 spaceborne lidar, *J. Geophys. Res. Biogeosci.*, 116, G04021,
1231 <https://doi.org/10.1029/2011jg001708>, 2011.
- 1232 Singh, R. S., Reager, J. T., Miller, N. L., and Famiglietti, J. S.: Toward hyper-resolution land-
1233 surface modeling: The effects of fine-scale topography and soil texture on CLM4.0 simulations
1234 over the Southwestern U.S., *Water Resour Res*, 51, 2648–2667,
1235 <https://doi.org/10.1002/2014wr015686>, 2015.
- 1236 Slingo, J., Bates, P., Bauer, P., Belcher, S., Palmer, T., Stephens, G., Stevens, B., Stocker, T.,
1237 and Teutsch, G.: Ambitious partnership needed for reliable climate prediction, *Nat Clim Change*,
1238 12, 499–503, <https://doi.org/10.1038/s41558-022-01384-8>, 2022.
- 1239 Still, C. J., Berry, J. A., Collatz, G. J., and DeFries, R. S.: Global distribution of C3 and C4
1240 vegetation: Carbon cycle implications, *Global Biogeochem Cy*, 17, 6-1-6–14,
1241 <https://doi.org/10.1029/2001gb001807>, 2003.
- 1242 Sulla-Menashe, D., Gray, J. M., Abercrombie, S. P., and Friedl, M. A.: Hierarchical mapping of
1243 annual global land cover 2001 to present: The MODIS Collection 6 Land Cover product, *Remote*
1244 *Sens Environ*, 222, 183–194, <https://doi.org/10.1016/j.rse.2018.12.013>, 2019.
- 1245 Swenson, S. C., Clark, M., Fan, Y., Lawrence, D. M., and Perket, J.: Representing Intrahillslope
1246 Lateral Subsurface Flow in the Community Land Model, *J Adv Model Earth Sy*, 11, 4044–4065,
1247 <https://doi.org/10.1029/2019ms001833>, 2019.
- 1248 Verdin, K. L. and Greenlee, S. K.: Development of continental scale digital elevation models and
1249 extraction of hydrographic features, paper presented at the Third International Workshop on
1250 Integrating GIS and Environmental Modeling, Santa Fe, New Mexico, 21–26 January, Natl.
1251 Cent. for Geogr. Inf. and Anal., Santa Barbara, Calif, 1996.
- 1252 Vergopolan, N., Chaney, N. W., Beck, H. E., Pan, M., Sheffield, J., Chan, S., and Wood, E. F.:
1253 Combining hyper-resolution land surface modeling with SMAP brightness temperatures to
1254 obtain 30-m soil moisture estimates, *Remote Sens Environ*, 242, 111740,
1255 <https://doi.org/10.1016/j.rse.2020.111740>, 2020.
- 1256 Vergopolan, N., Chaney, N. W., Pan, M., Sheffield, J., Beck, H. E., Ferguson, C. R., Torres-
1257 Rojas, L., Sadri, S., and Wood, E. F.: SMAP-HydroBlocks, a 30-m satellite-based soil moisture
1258 dataset for the conterminous US, *Sci Data*, 8, 264, <https://doi.org/10.1038/s41597-021-01050-2>,
1259 2021.
- 1260 Vergopolan, N., Sheffield, J., Chaney, N. W., Pan, M., Beck, H. E., Ferguson, C. R., Torres-
1261 Rojas, L., Eigenbrod, F., Crow, W., and Wood, E. F.: High-Resolution Soil Moisture Data

Deleted: Journal of Geophysical Research: Biogeosciences,

1263 Reveal Complex Multi-Scale Spatial Variability Across the United States, *Geophys Res Lett*, 49,
1264 <https://doi.org/10.1029/2022gl098586>, 2022.

1265 Wood, E. F., Roundy, J. K., Troy, T. J., Beek, L. P. H. van, Bierkens, M. F. P., et al.:
1266 Hyperresolution global land surface modeling: Meeting a grand challenge for monitoring Earth's
1267 terrestrial water, *Water Resour Res*, 47, <https://doi.org/10.1029/2010wr010090>, 2011.

1268 Xia, Y., Mocko, D., Huang, M., Li, B., Rodell, M., Mitchell, K. E., Cai, X., and Ek, M. B.:
1269 Comparison and Assessment of Three Advanced Land Surface Models in Simulating Terrestrial
1270 Water Storage Components over the United States, *J Hydrometeorol*, 18, 625–649,
1271 <https://doi.org/10.1175/jhm-d-16-0112.1>, 2017.

1272 [Xu, C., Torres-Rojas, L., Vergopolan, N., Chaney, N. W.: The Benefits of Using State-Of-The-
1273 Art Digital Soil Properties Maps to Improve the Modeling of Soil Moisture in Land Surface
1274 Models, *Water Resour Res*, 59\(4\), e2022WR032336, <https://doi.org/10.1029/2022WR032336>,
1275 2023.](#)

1276 [Yang, Z. L., Niu, G. Y., Mitchell, K. E., Chen, F., Ek, M. B., Barlage, M., et al.: The community
1277 Noah land surface model with multiparameterization options \(Noah-MP\): 2. Evaluation over
1278 global river basins, *J Geophys Res Atmos*, 116\(D12\), <https://doi.org/10.1029/2010JD015140>,
1279 2011.](#)

1280 Yamazaki, D., Ikeshima, D., Sosa, J., Bates, P. D., Allen, G. H., and Pavelsky, T. M.: MERIT
1281 Hydro: A High-Resolution Global Hydrography Map Based on Latest Topography Dataset,
1282 *Water Resour Res*, 55, 5053–5073, <https://doi.org/10.1029/2019wr024873>, 2019.

1283 Yang, C. and Zhao, S.: A building height dataset across China in 2017 estimated by the spatially-
1284 informed approach, *Sci Data*, 9, 76, <https://doi.org/10.1038/s41597-022-01192-x>, 2022.

1285 Yuan, H., Dai, Y., Xiao, Z., Ji, D., and Shangguan, W.: Reprocessing the MODIS Leaf Area
1286 Index products for land surface and climate modelling, *Remote Sens Environ*, 115, 1171–1187,
1287 <https://doi.org/10.1016/j.rse.2011.01.001>, 2011.

1288 Yuan, X., Ji, P., Wang, L., Liang, X., Yang, K., Ye, A., Su, Z., and Wen, J.: High-Resolution
1289 Land Surface Modeling of Hydrological Changes Over the Sanjiangyuan Region in the Eastern
1290 Tibetan Plateau: 1. Model Development and Evaluation, *J Adv Model Earth Sy*, 10, 2806–2828,
1291 <https://doi.org/10.1029/2018ms001412>, 2018.

1292 Zeng, X., Shaikh, M., Dai, Y., Dickinson, R. E., and Myneni, R.: Coupling of the Common Land
1293 Model to the NCAR Community Climate Model, *J Climate*, 15, 1832–1854,
1294 [https://doi.org/10.1175/1520-0442\(2002\)015<1832:cotclm>2.0.co;2](https://doi.org/10.1175/1520-0442(2002)015<1832:cotclm>2.0.co;2), 2002.

1295 Zhao, M., Cheng, C., Zhou, Y., Li, X., Shen, S., and Song, C.: A global dataset of annual urban
1296 extents (1992–2020) from harmonized nighttime lights, *Earth Syst Sci Data*, 14, 517–534,
1297 <https://doi.org/10.5194/essd-14-517-2022>, 2022.

Deleted: Vrese, P. de, Schulz, J.-P., and Hagemann, S.: On the Representation of Heterogeneity in Land-Surface–Atmosphere Coupling, *Bound-lay Meteorol*, 160, 157–183, <https://doi.org/10.1007/s10546-016-0133-1>, 2016.

1302 Zhou, Y., Li, D., and Li, X.: The Effects of Surface Heterogeneity Scale on the Flux Imbalance
1303 under Free Convection, *J Geophys Res Atmospheres*, 124, 8424–8448,
1304 <https://doi.org/10.1029/2018jd029550>, 2019.

Page 9: [1] Deleted Li, Lingcheng 1/3/24 1:46:00 AM

Page 9: [2] Deleted Li, Lingcheng 1/3/24 1:46:00 AM